SEDIMENTOLOGY the journal of the International Association of Sedimentologists

*Sedimentology* (2012) **59,** 809–829 doi: 10.1111/j.1365-3091.2011.01280.x

# Petrology and geochemistry of chert on the marginal zone of Yangtze Platform, western Hunan, South China, during the Ediacaran–Cambrian transition

JIANGUO WANG*, DAIZHAO CHEN*, DAN WANG*, DETIAN YAN†, XIQIANG ZHOU* and QINGCHEN WANG†

**Key Laboratory of Petroleum Resources Research, Institute of Geology and Geophysics, Chinese Academy of Sciences, P. O. Box 9825, Beijing 100029, China (E-mail: dzh-chen@mail.iggcas.ac.cn)*

*†State Key Laboratory of Lithospheric Evolution, Institute of Geology and Geophysics, Chinese Academy of Sciences, P.O. Box 9825, Beijing 100029, China*

Associate Editor – Adrian Immenhauser

## ABSTRACT

The Ediacaran–Cambrian transition was one of the most critical intervals in Earth history. During this interval, widespread chert was precipitated, commonly as a stratal wedge in carbonates, along the southern margin of the Yangtze Platform, South China. The chert wedge passes into a full chert succession further basinward to the south-east. Four lithotypes of chert are identified across the marginal zone in western Hunan: mounded, vein, brecciated and bedded chert. The mounded chert is characterized by irregular to digitiform internal fabrics, generally with abundant original vesicles and/or channels that mostly are lined by botryoidal chalcedony cements with minor quartz and barite crystals. The host chert (or matrix) of these mounds is dominated by amorphous cryptocrystalline silica, commonly disseminated with pyrite. The vein chert, with minor quartz locally, generally cross-cuts the overlying dolostone and chert horizons and terminates under the mounded and/or bedded chert bodies. The brecciated chert commonly occurs as splayed 'intrusions' or funnel-shaped wedges and cross-cuts the topmost dolostones. The bedded chert, the most common type, generally is thin to medium-bedded and laminated locally; it is composed of amorphous silica with minor amounts of black lumps. Microthermometry of fluid inclusions from vein and void-lining minerals (mainly quartz and barite) revealed homogenization temperatures from 120 to 180°C for the trapped primary fluids. Compositionally, these chert deposits generally are pure, with $SiO_2 > 92$ wt%, and only minor $Fe_2O_3$ and $Al_2O_3$ contents, most of which show positive Europium anomalies in rare earth element patterns, especially for the mounded chert. All these data suggest that the marginal zone chert deposits resulted from a low-temperature, silica-rich hydrothermal system, in which the mounded chert was precipitated around the releasing vents, i.e. as silica chimneys. The vein and splayed brecciated chert, however, was formed along the syndepositional fault/fracture conduits that linked downward, while the bedded chert was precipitated in the quieter water column from the fallout of hydrothermal plumes onto the sea floor. These petrological and geochemical data provide compelling evidence and a new clue to the understanding of the extensive silica precipitation; rapid tectono-depositional and oceanic changes during the Ediacaran–Cambrian transition in South China.

**Keywords** Chert, Ediacaran–Cambrian, hydrothermal activity, platform margin, silica chimney, South China.

## INTRODUCTION

The Ediacaran–Cambrian (E–C) transition was a critical time in Earth history marked by dramatic changes in the biotic realm, i.e. the disappearance of Ediacaran biota and subsequent explosive bioradiation of metazoans in the Early Cambrian (Brasier, 1995; Grotzinger *et al.*, 1995; Amthor *et al.*, 2003; Steiner *et al.*, 2007) and ocean chemistry (Shen & Shidlowski, 2000; Kimura & Watanabe, 2001; Goldberg *et al.*, 2005; Schröder & Grotzinger, 2007). Extensive black chert successions of the Liuchapo Formation (or equivalents), overlain by thick black shale series of the Niutitang Formation (or equivalents), commonly occur in the E–C successions off the northern and southern flanks of the Yangtze Platform (Zhu *et al.*, 2003; Fig. 1A). Compared with the Niutitang polymetallic black shales, less attention has been paid to the Liuchapo chert deposits, and thus their origins were even more poorly constrained. This scenario is not favourable for a complete understanding of the vast oceanic changes which occurred during the E–C transition. Based mainly on geochemical data, both hydrothermal (Peng *et al.*, 1995; Li & Gao, 1996; Li, 1997; Jiang & Li, 2005) and marine (biogenic) processes (Tang *et al.*, 1997; Guo *et al.*, 2007) have been proposed as causative mechanisms. Geological evidence of hydrothermal origin, although noticed by some earlier researchers (Li, 1997), has not been further investigated and reasonably documented.

The platform to basin transition zone is a key area sensitive to oceanic changes both in shallow and deep-water regimes. In a previous study, although a few lines of petrological evidence for the hydrothermal-originated Liuchapo chert deposits (silica chimneys) across the marginal zone of the Middle Yangtze Platform near Dayong (or Zhangjiajie) in western Hunan, South China were reported (Chen *et al.*, 2009; Fig. 1), they were neither well-documented nor interpreted in detail. In this paper, additional petrological evidence for these specific chert deposits, together with microthermometric and geochemical data, is provided to refine the origin of the extensive chert deposits and to better understand the vast environmental and biotic turnovers during the E–C transition. All these data further support the hydrothermal origin for the E–C chert deposits across the marginal zone.

## GEOLOGICAL SETTING

During the E–C transition, the Yangtze Block gradually evolved from a rift to a passive continental margin basin (Wang & Li, 2003), most of which was covered by carbonate platforms that evolved from the early Ediacaran (Doushantuo) rimmed carbonate platform system (Vernhet & Reijmer, 2010; Jiang *et al.*, 2011). These platforms were surrounded by narrow margin-slope zones on the northern flank (*ca* 900 km long) and south to south-western flank (≥1600 km long; Fig. 1A). The southern margin-slope of the Yangtze platforms (Fig. 1A) extended approximately along the antecedent Jinningian (*ca* 1·0 to 0·8 Ga) orogenic zone (or Jiangnan orogen) between the Yangtze and Cathaysia blocks (Li, 1999; Zheng *et al.*, 2008). From the late Ediacaran (*ca* 551 Ma), widespread chert, rather than carbonates, was deposited simultaneously in deeper environments off platform margins and further basinward, including in intraplatform basins (Zhu *et al.*, 2003; Fig. 1A). These carbonate platforms subsequently were drowned in the Early Cambrian.

This study focuses on the chert successions across the marginal zone of the Middle Yangtze Platform near Dayong in western Hunan, South China (Fig. 1). On this platform, the shallow water E–C successions include the Dengying Formation, composed mostly of stromatolitic and/or algal dolostones, and the overlying Niutitang Formation (or equivalents), composed of a basal phosphorite-rich (locally with a polymetallic Ni-Mo-PGE sulphide bed) horizon and an upper black shale succession up to several hundred metres thick. The correlative 'deep-water' E–C sections include the Liuchapo Formation (or equivalents), composed mainly of bedded to massive chert deposits (*ca* 10 m up to *ca* 100 m thick), which is also overlain by the Niutitang Formation (Fig. 2). This siliceous formation is a diachronous stratigraphic unit, deposited earlier

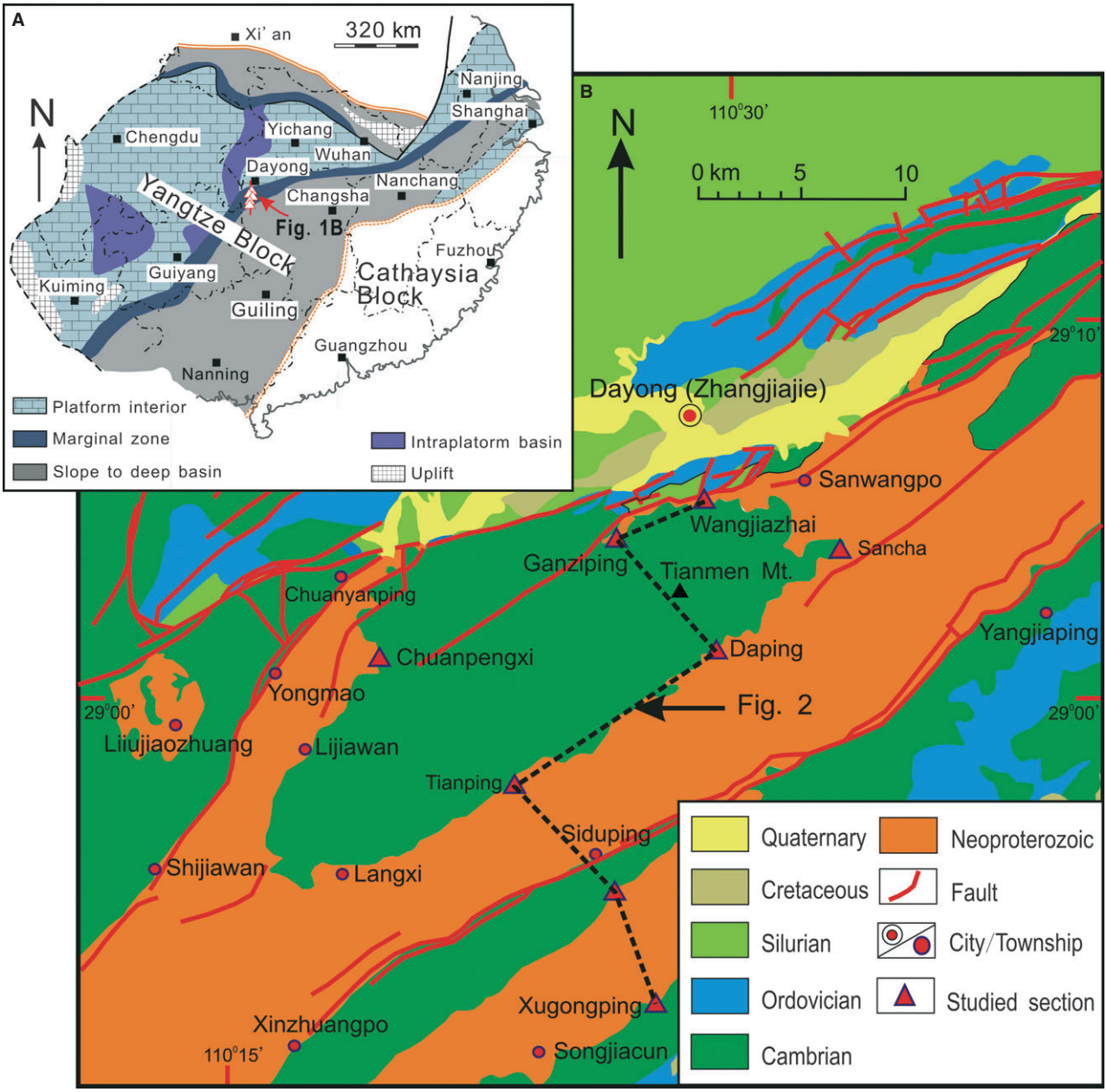


**Fig. 1.** (A) Simplified palaeogeographic map of the Yangtze Block during the Ediacaran–Cambrian transition, illustrating the geological setting of the study area. (B) Geological map near Dayong in western Hunan, South China. The dashed line shows the location of the stratigraphical transect in Fig. 2.

in the deeper, basinward environment (Chen *et al.*, 2009). The boundary demarcating the Ediacaran and Cambrian systems was placed tentatively within the Liuchapo Formation in the deeper slope to basin setting (Zhu *et al.*, 2003). Based on zircon U-Pb isotopic dating and carbon isotopic stratigraphy (Chen *et al.*, 2009; Fig. 2), it is proposed that the E–C boundary be further defined and placed near the base of the Liuchapo Formation toward the carbonate platform margin.

## METHODS

Detailed outcrop investigation, descriptions and microscopic examinations were carried out first to characterize the occurrence and petrology of the Liuchapo chert on the south-eastern margin of the Middle Yangtze Platform (see Fig. 1 for the locations of studied sections). Then microthermometric measurement of fluid inclusions was conducted on selected doubly polished wafers to determine the properties of fluids from which the

 

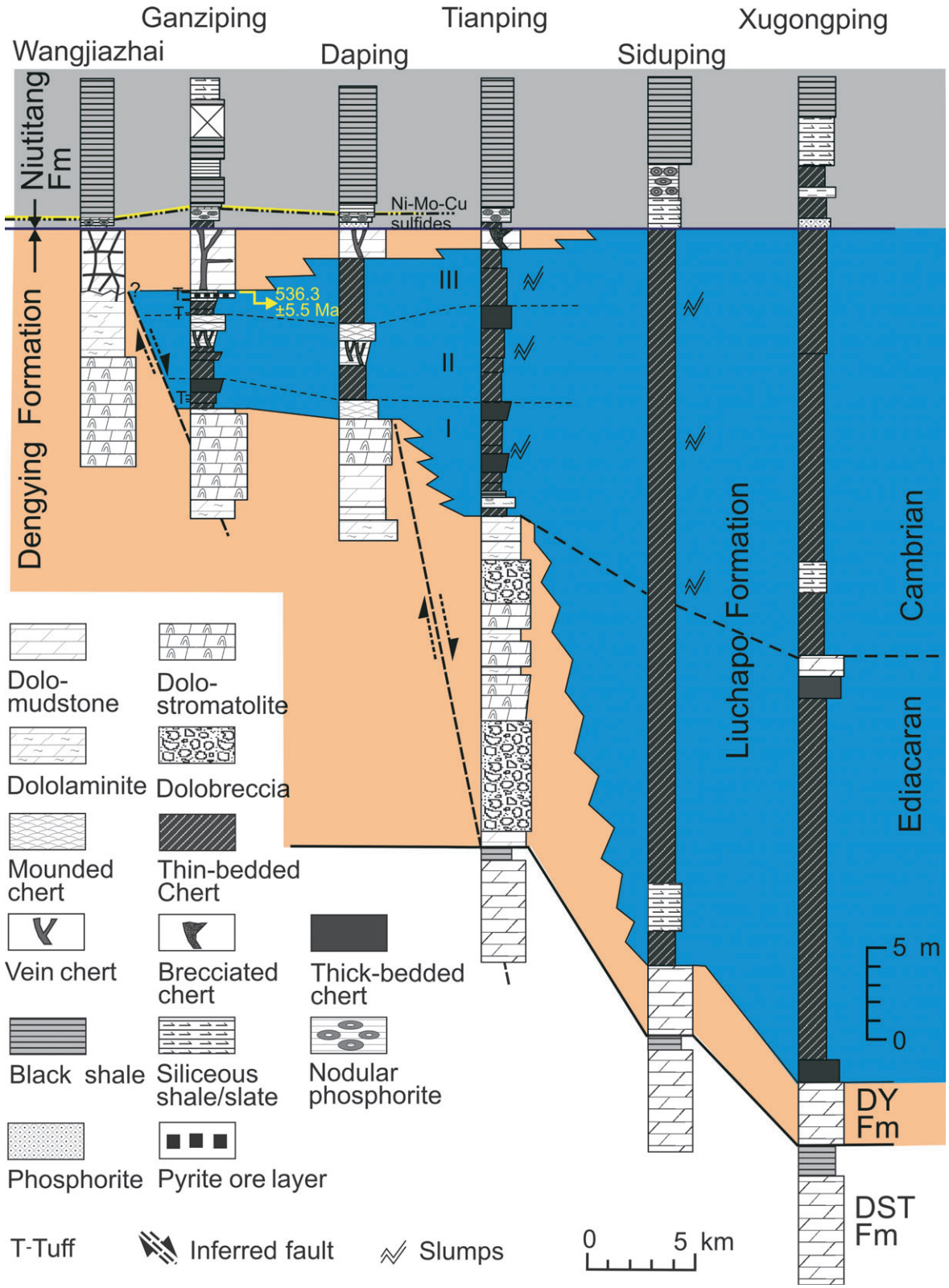


**Fig. 2.** Cross-section showing stratigraphic and lithofacies changes straddling the Ediacaran–Cambrian boundary from the platform to the margin on the southern flank of the Yangtze Platform near Dayong (or Zhangjiajie), western Hunan, South China (modified from Chen *et al.*, 2009). Three episodes of hydrothermal venting (I, II and III) can be identified approximately in the study area. DST Fm = Doushantuo Formation, DY Fm = Dengying Formation. Age data from Chen *et al.* (2009). See Fig. 1 for the location.

silica precipitated. To minimize the effect of re-equilibration on the homogenization temperatures ($T_h$), the fluid inclusion assemblage (FIA), defined as a group of inclusions along a single growth zone with consistent vapour/liquid ratios (Goldstein & Reynolds, 1994), was applied in microthermometric measurement. The accuracy of $T_h$ values and final melting temperature of ice ($T_m$) is within 0·5°C and 3°C, respectively. Salinity is calculated using $T_m$ values and is expressed as wt% NaCl equivalent (Bodnar, 1993): wt% NaCl = $1{\cdot}78 \times T_m - 0{\cdot}0442 \times T^2_m + 0{\cdot}000557 \times T^3_m$.

After petrographic examination, different types of chert from each of the studied localities (Fig. 1B) were selected and separately powdered for geochemical analyses. Major elements were analysed using an automatic X-ray fluorescence spectrometer (Shimadzu XRF-1500; Shimadzu Corporation, Kyoto, Japan) using fusion glasses made from a mixture of powdered sample and flux ($Li_2B_4O_7$) in the proportion of 1 : 8. The precision and accuracy of the major-element data are ≤3% and *ca* 5% ($2\sigma$), respectively. X-ray diffraction analysis was conducted to assess the non-silica minerals present in the chert. Samples (powder) for trace elements, including rare earth element (REE) analysis, were first digested with $HNO_3$-HF-$HCLO_4$ solution in sealed Teflon® beakers, then the dissolved solution was introduced into the inductively coupled plasma mass spectrometer (Finnigan Element ICP-MS; Thermo Scientific, West Palm Beach, FL, USA) for analysis. Precision for all trace elements is estimated to be 5% and accuracy is better than 5% for most elements, detection limits for almost REE are 0·1 parts-per-billion (ppb) in concentration. All analyses were carried out at the Institute of Geology and Geophysics, Chinese Academy of Sciences.

To avoid analytical interference on calculations of Europium (Eu) anomalies caused by Ba concentrations in ICP-MS analysis, corrections according to the method of Dulski (1994) were applied: $Eu/Eu^* = (3 \times Eu_n)/(2 \times Sm_n + Tb_n)$. Cerium (Ce/Ce*) and Praseodymium (Pr/Pr*) anomalies were calculated according to the method of Bau & Duski (1996): $Ce/Ce^* = Ce_n/(0{\cdot}5La_n + 0{\cdot}5Pr_n)$, $Pr/Pr^* = Pr_n/(0{\cdot}5Ce_n + 0{\cdot}5Nd_n)$, using shale PAAS-normalized abundances. The 'n' refers to normalized concentrations against the shale standard PAAS (Taylor & McClennan, 1985; McLennan, 1989). The degree of light REEs (LREEs) enrichment relative to heavy REEs (HREEs) is presented as the ratio of shale-normalized La to Yb ($La_n/Yb_n$).

## RESULTS

### Petrology of chert

The study area was geologically located across the marginal zone of the Middle Yangtze Platform near Dayong (or Zhangjiajie), western Hunan in South China (Fig. 1). Stratigraphic correlation across the depositional strike (from Wangjiazhai to Ganziping, Daping, Tianping, Siduping and Xugongping) demonstrates that shallow-water Dengying dolostones along the platform margin sharply pass basinward into Liuchapo chert deposits which occur as a stratal wedge embedded in the carbonate successions; this chert wedge thickens rapidly and passes basinward into a complete chert succession (Chen *et al.*, 2009; Fig. 2). Detailed observations across the marginal zone enable four types of chert to be recognized within the chert wedge: (i) mounded; (ii) vein; (iii) brecciated; and (iv) bedded chert.

#### *Mounded chert*

Mounded chert is present in the mid-upper horizon of Liuchapo Formation at Ganziping and the mid-lower part at Daping (Fig. 2). This facies, commonly 0·5 to 2 m thick, is characterized by mounded or domal surfaces on the top (Fig. 3A and B). These mounds, generally 20 to 50 cm across and <30 cm in relief, occur either individually or as laterally linked clusters, upon which remnant vents are preserved locally (Fig. 3B). The well-preserved silica mounds commonly exhibit irregular spongy (or honeycombed) to digitate internal fabrics (Fig. 3C to E), locally with interconnected channels and veins (Fig. 3F). Abundant vesicles/voids were present within the mounds although they were mostly plugged by botryoidal fibrous (length-fast) chalcedony (commonly recrystallized), and radiating micro-quartz to macro-quartz crystals with minor lath-like (bladed) barite, pyrite and saddle dolomite (Figs 3C to F and 4A to C). The host chert (or matrix) is dominated by amorphous to cryptocrystalline silica, in which silicified Fe-oxyhydroxide shrubs are preserved locally. The matrix is commonly impregnated with irregular or idiomorphic Fe-sulphides or their alteration products (i.e. hematite; Figs 3E and 4D), especially along the channel walls (Fig. 3F). Rare sanidine, muscovite and volcanic glass (cryptocrystalline) fragments (platy, cuspate and crescent glass shards) were identified within the matrix of silica mounds (Fig. 4E).

 

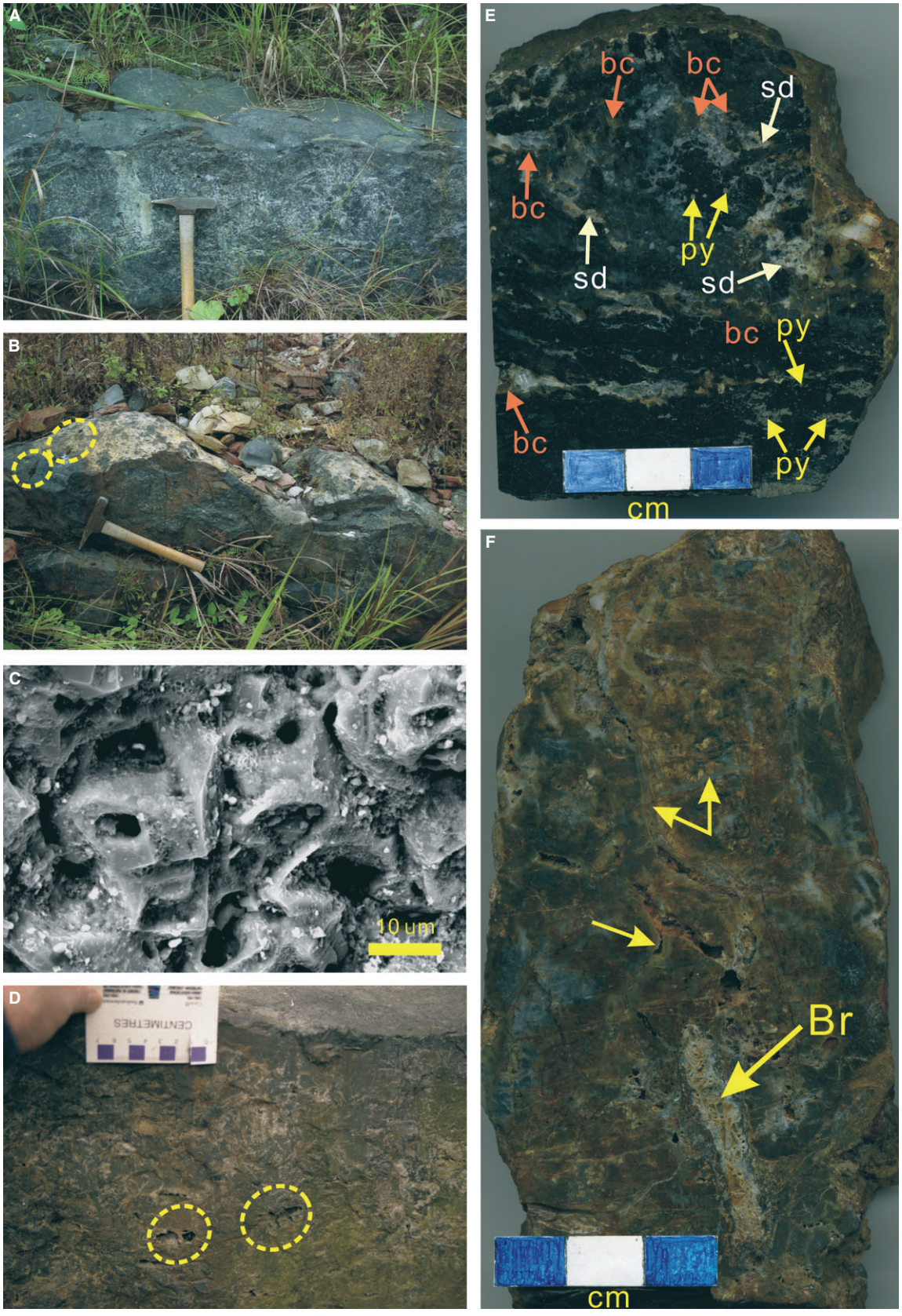
A
B
C
10 um
D
CENTIMETRES
E
bc
bc
sd
bc
py
sd
sd
bc
py
bc
py
cm
F
Br
cm

**Fig. 3.** (A) Mounded chert horizon exhibited by the domal surface and spongy internal fabrics in which abundant vesicles are filled mainly by barite and quartz. Ganziping. Hammer for scale (35 cm long). (B) Relict venting spouts on the surface of a chert mound (circle). Hammer for scale (35 cm long). (C) Scanning electron microscope photomicrograph showing honeycomb-like fabrics of chert within a silica mound. Ganziping. (D) Irregular to digitiform fabrics in the silica mound, abundant voids and/or conduits, some still open (circle). Ganziping. (E) Polished slab showing irregular to spongy internal fabrics within the silica mound, abundant original voids and vent conduits mostly plugged by saddle dolomite 'sd', botryoidal chalcedony 'bc' and quartz cements. The silica matrix consists of dark grey amorphous to cryptocrystalline silica impregnated with abundant irregular pyrite crystals 'py'. Ganziping. (F) Polished slab showing tortuous, interwoven vent channels lined with radiating fibrous agate crusts (or chalcedony) (arrows) in the silica mound. Note the minor bladed barite crystals 'Br' within the channel and abundant Fe sulphides in the silica host (altered to hematite due to later oxidation). Daping (from Chen *et al.*, 2009).

*Vein chert*

Vein chert, generally 1 to 10 cm wide, is preserved in the dolostones as vein/fracture infills in the middle and/or the top carbonates above the chert wedge at Ganziping and Daping (Fig. 2). Vein infills mainly comprise cryptocrystalline silica (chert), with minor quartz crystals locally. The chert-filling veins are found to cross-cut the dolostones sub-vertically, and terminate under those mounded and/or bedded chert facies (Fig. 2); they are laterally linked to the interbedded chert veins, forming complicated vein networks (Fig. 4F).

*Brecciated chert*

Brecciated chert occurs where the uppermost dolostones are present, i.e. at Tianping (Fig. 2). This facies sub-vertically cross-cuts the uppermost dolostones and is overlain directly by the Niutitang phosphorite-rich shales, commonly forming splayed/funnelled brecciated 'intrusive bodies' (Fig. 4G). Such silica 'intrusions' locally occurred closely as clusters (spaced 5 to 8 m apart). The breccias generally are angular in shape and composed of cryptocrystalline silica, within which micro-fissures, lined with quartz, dolomite and rare barite, are extensive.

*Bedded chert*

Bedded chert is the most common type among the chert facies in the studied sections and tends to be the exclusive one further basinward (Fig. 2). This facies generally is thin to medium-bedded, locally thick-bedded (>30 cm in bed thickness). The thin-bedded chert generally bears horizontal fine lamination indicated by compositional alternations, but the medium-bedded and thick-bedded chert commonly shows weak to no lamination. Slumps and/or intraformational truncation are present generally in the thin-bedded chert at the outer part of the chert wedge, i.e. at Tianping and further basinward (Fig. 2). The lithology is composed mainly of amorphous cryptocrystalline silica with minor amounts of black lumps (or aggregates) (probably organic matter). Rare silicified worm-like fossil remains (Fig. 4H) are present within this type of chert, particularly at the base of chert successions. Several thin, tuffaceous beds (generally <5 cm) are intercalated within the thin-bedded chert horizons.

## Fluid inclusion microthermometry

Two-phase (liquid-vapour) primary aqueous FIAs were observed along growth zones of relatively coarse-crystalline void/vein-lining quartz and barite crystals. However, rare, even single-phase aqueous, fluid inclusions were observed in the earlier void/vein-lining botryoidal chalcedony. Fluid inclusions, with vapour/fluid ratios of 5 to 10%, generally are small (3 to 8 μm) in size and variable (oval, elongate or irregular) in shape. Each FIA has relatively consistent $T_h$ and $T_m$ values, suggesting minimal re-equilibration.

In this study, microthermometry was conducted on samples derived from Daping and Ganziping (Fig. 5A to D). At Daping (Fig. 5A and C), channel-lining equant quartz crystals (see Fig. 4A) yield $T_h$ values of 120 to 146°C (average 130°C) and $T_m$ values of −17·1 to −12·9°C (average −15·0°C). The salinity, estimated from $T_m$ values, varies from 16·8 to 20·3 wt% NaCl equivalent (average 18·6%). Channel-filling bladed barites (see Fig. 3F) yield $T_h$ values of 125 to 141°C (average 134·7°C) and $T_m$ values of −22·2 to −18·1°C (average −20·2°C). The salinity varies from 21·1 to 23·8 wt% NaCl equivalent (average 22·5%). At Ganziping (Fig. 5B and D), prismatic quartz crystals in the chert vein (upper part of Fig. 4F) have $T_h$ values of 141 to 177°C (average 159·5°C), $T_m$ values between −20·5°C and −16·4°C (average −18·9°C), and salinity from 19·8 to 22·7 wt% NaCl equivalent (average 21·6%). No fluid

 

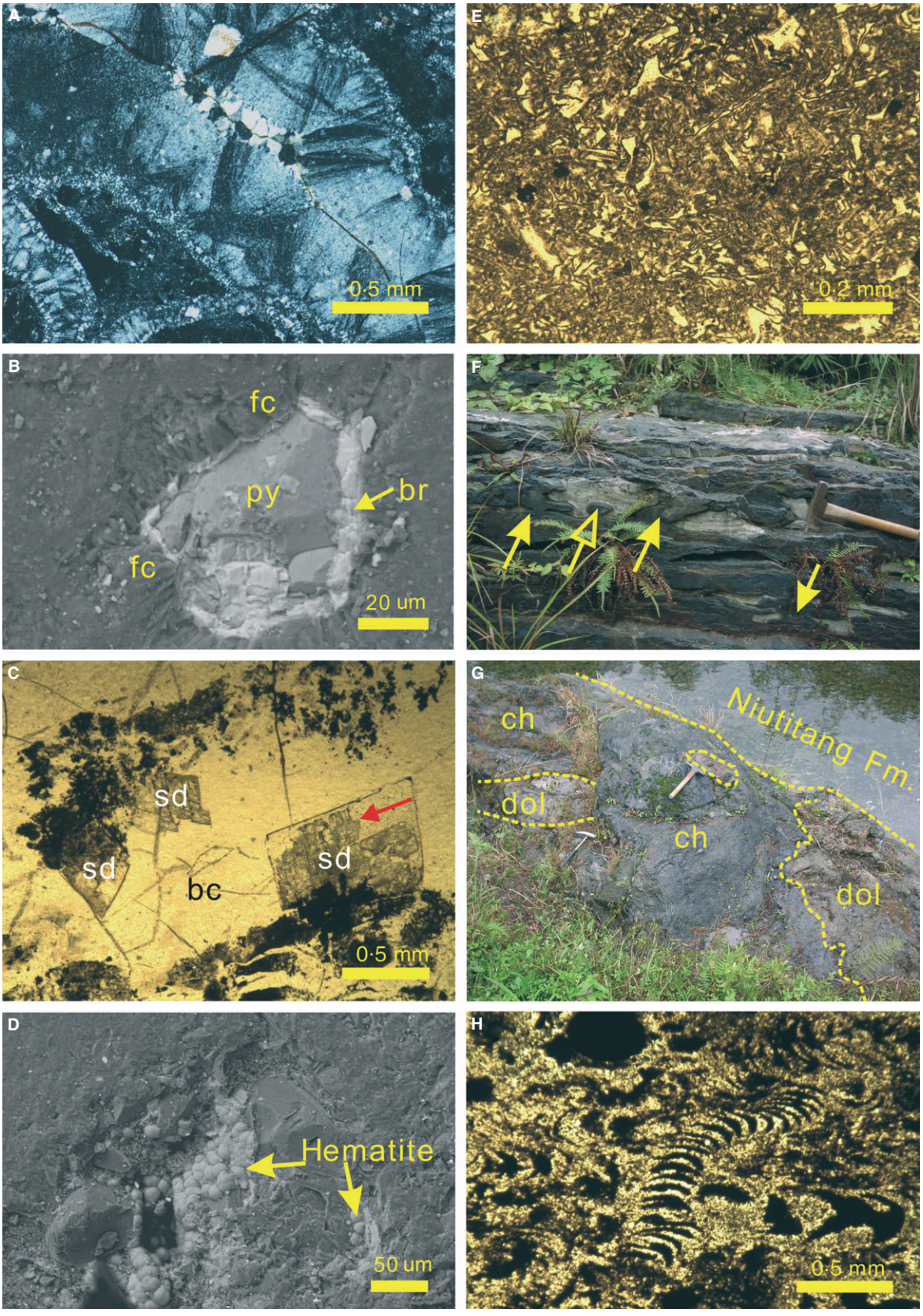
A
0·5 mm
E
0·2 mm
B
fc
py
br
fc
20 um
F
C
sd
sd
sd
bc
0·5 mm
G
ch
Niutitang Fm.
dol
ch
dol
D
Hematite
50 um
H
0·5 mm

**Fig. 4.** (A) A micro-vein/channel in an amorphous silica host filled by three generations of silica cements in order: (i) thin microcrystalline bladed quartz crusts; (ii) cryptocrystalline fibrous chalcedony (or agate) cements (spherolitic extinction); and (iii) micro-crystalline to meso-crystalline quartz mosaics in the centre. Ganziping. Cross-polarized light. (B) Scanning electron microscope (SEM) photomicrograph showing a vesicle/void plugged by three generations of cements in order: (i) fibrous chalcedony 'fc'; (ii) barite 'br'; and (iii) pyrite crystal 'py'. Daping. (C) Photomicrograph showing veins/voids cemented by saddle dolomite 'sd' and botryoidal chalcedony 'bc' and microquartz crystals (light-coloured areas). Note the dolomite corrosion by the silica (arrow) and the Fe-oxyhydroxide shrubs in the silica host. Ganziping. Plane-polarized light. (D) SEM photomicrograph showing kidney-shaped Fe oxide (hematite) in the quartz-lining void and on the surface. Daping. (E) Volcanic glasses in the chert mound, characterized by amorphous glass shards and devitrified glasses. Ganziping. Plane-polarized light. (F) Black chert head intruded upward into (hollow arrow) and finally cross-cutting the thin-bedded dolostones (solid arrows), leading to progressive corrosion and/or replacement of dolostones. Ganziping. Hammer for scale (35 cm long). (G) Brecciated 'intrusive chert body' cross-cutting the overlying dolostone 'dol' and splaying sub-vertically. Note the chert breccias and silicified dolobreccia (within the circle) in the 'intrusive' chert unit. 'ch' = chert. Tianping (from Chen *et al.*, 2009). Hammer is 35 cm long. (H) Silicified worm-like fossils (*Palaeopascichnus jiumenensis*, cf. Dong *et al.*, 2008) preserved in the basal bedded chert. Ganziping. Plane-polarized light.

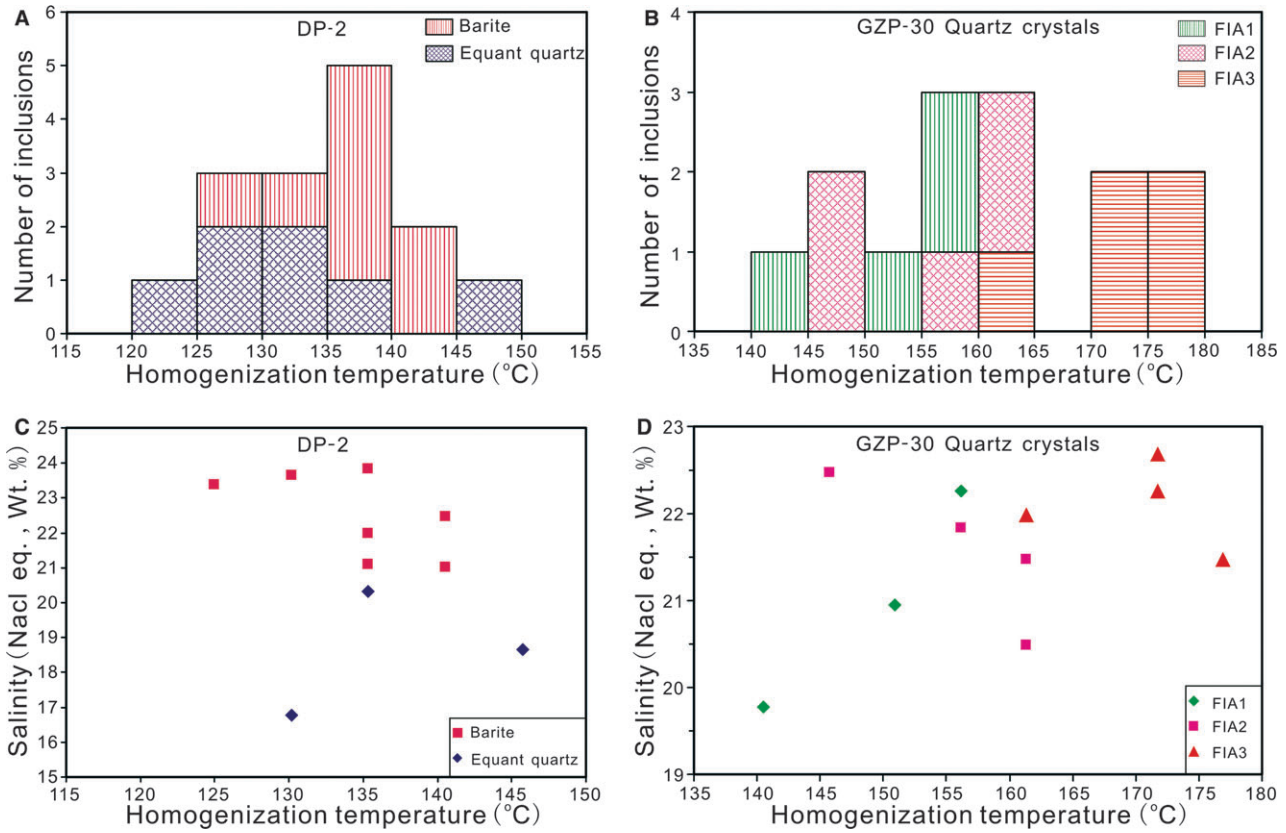


**Fig. 5.** Microthermometric data of primary fluid inclusions. (A) Histogram of homogenization temperatures ($T_h$) of fluid inclusions in quartz and barite crystals from Daping. (B) Histogram of $T_h$ of fluid inclusions in quartz from Ganziping. (C) Cross-plots of $T_h$ and salinity (NaCl wt% equivalent) of fluid inclusions from Daping. (D) Cross-plots of $T_h$ and salinity of fluid inclusions from Ganziping. FIA = fluid inclusion assemblage.

inclusion data was obtained from the botryoidal chalcedony for this study.

## Element geochemistry

Major and trace element (including REE) concentrations for the Liuchapo chert are presented in Tables 1 and 2. In general, all of the chert types are dominated by $SiO_2$ (generally 92 to 97%), with minor contributions from total Fe-oxides (denoted as $TFe_2O_3$; 0·34 to 7·14%) and $Al_2O_3$ (0·04 to 2·74), and extremely low contents of $TiO_2$ (<0·12%). There is no significant variation in $SiO_2$ content among the different types of chert, except

**Table 1.** Major element contents (wt%) in the chert across the Ediacaran–Cambrian boundary succession, western Hunan in South China.

| Sample | Chert facies | $SiO_2$ | $TiO_2$ | $Al_2O_3$ | $TFe_2O_3$* | MnO | MgO | CaO | $Na_2O$ | $K_2O$ | $P_2O_5$ | LOI | Total | Fe/Ti | Al/(Al + Fe) |
|---|---|---|---|---|---|---|---|---|---|---|---|---|---|---|---|
| GZP04 | Mounded chert | 96·00 | 0·04 | 0·74 | 1·31 | <0·01 | 0·20 | 0·26 | 0·19 | 0·21 | 0·01 | 1·30 | 100·26 | 38·21 | 0·36 |
| GZP04C | Mounded chert | 84·96 | 0·05 | 1·91 | 7·14 | <0·01 | 0·27 | 0·08 | 0·01 | 0·69 | 0·05 | 4·81 | 99·98 | 157·47 | 0·21 |
| GZP04CR | Mounded chert | | | | | | | | | | | | | | |
| GZP04E | Mounded chert | 90·66 | 0·04 | 0·57 | 2·47 | <0·01 | 0·32 | 2·88 | <0·01 | 0·21 | 0·01 | 2·26 | 99·42 | 72·04 | 0·19 |
| DP2 | Mounded chert | 94·38 | 0·08 | 0·59 | 3·12 | <0·01 | 0·14 | 0·04 | 0·01 | 0·15 | 0·05 | 0·86 | 99·42 | 45·50 | 0·16 |
| Average values | | 91·50 | 0·05 | 0·95 | 3·51 | | | | | | | | | 78·30 | 0·23 |
| GZP26' | Vein chert | 93·79 | 0·06 | 1·33 | 1·70 | <0·01 | 0·17 | 0·06 | 0·08 | 0·45 | 0·01 | 2·13 | 99·78 | 33·06 | 0·44 |
| GZP29' | Vein chert | 89·59 | 0·12 | 2·49 | 2·90 | <0·01 | 0·38 | 0·07 | 0·10 | 0·87 | 0·02 | 3·28 | 99·82 | 28·19 | 0·46 |
| GZP30'W | Vein chert | 98·71 | <0·01 | 0·01 | 0·56 | <0·01 | 0·16 | 0·17 | 0·06 | 0·01 | 0·01 | 0·02 | 99·71 | 65·33 | 0·02 |
| Average values | | 94·03 | 0·06 | 1·28 | 1·72 | | | | | | | | | 42·19 | 0·31 |
| TP27 | Brecciated chert | 96·75 | 0·04 | 0·99 | 0·69 | <0·01 | 0·10 | 0·03 | 0·02 | 0·55 | 0·01 | 0·26 | 99·44 | 20·13 | 0·59 |
| TP28 | Brecciated chert | 96·48 | 0·04 | 0·99 | 0·86 | <0·01 | 0·09 | 0·03 | 0·01 | 0·56 | 0·01 | 0·44 | 99·51 | 25·08 | 0·54 |
| TP31 | Brecciated chert | 95·93 | <0·01 | 0·59 | 0·28 | <0·01 | 0·24 | 0·53 | 0·05 | 0·15 | 0·14 | 1·70 | 99·61 | 32·67 | 0·68 |
| TP33 | Brecciated chert | 95·94 | 0·01 | 0·02 | 0·48 | <0·01 | 0·09 | 0·08 | 0·08 | 0·03 | 0·02 | 2·76 | 99·51 | 56·00 | 0·04 |
| TP37 | Brecciated chert | 95·29 | 0·03 | 0·71 | 0·61 | <0·01 | 0·47 | 0·67 | 0·01 | 0·43 | 0·06 | 1·22 | 99·50 | 23·72 | 0·54 |
| Average values | | 96·08 | 0·02 | 0·66 | 0·58 | | | | | | | | | 31·52 | 0·48 |
| GZP12' | Bedded chert | 92·81 | 0·08 | 2·07 | 1·16 | <0·01 | 0·33 | 0·38 | 0·09 | 0·82 | 0·08 | 1·88 | 99·70 | 16·92 | 0·64 |
| GZP17' | Bedded chert | 95·70 | 0·05 | 1·12 | 0·67 | <0·01 | 0·10 | 0·08 | 0·12 | 0·43 | 0·01 | 1·25 | 99·53 | 15·63 | 0·63 |
| GZP22' | Bedded chert | 96·62 | 0·03 | 0·74 | 0·57 | <0·01 | 0·06 | 0·07 | 0·08 | 0·35 | 0·01 | 0·93 | 99·46 | 22·17 | 0·56 |
| GZP24' | Bedded chert | 96·56 | 0·03 | 0·91 | 0·79 | <0·01 | 0·05 | 0·05 | 0·08 | 0·36 | 0·01 | 1·07 | 99·91 | 30·72 | 0·54 |
| GZP25' | Bedded chert | 93·86 | 0·08 | 1·87 | 1·09 | <0·01 | 0·23 | 0·05 | 0·14 | 0·64 | 0·01 | 1·77 | 99·74 | 15·90 | 0·63 |
| DP5 | Bedded chert | 92·20 | 0·09 | 2·74 | 0·64 | <0·01 | 0·22 | 0·06 | 0·09 | 1·37 | 0·01 | 2·63 | 100·05 | 8·30 | 0·81 |
| DP6B | Bedded chert | 94·15 | 0·05 | 1·85 | 0·70 | <0·01 | 0·21 | 0·04 | 0·03 | 0·88 | 0·01 | 1·58 | 99·50 | 16·33 | 0·73 |
| DP7 | Bedded chert | 92·89 | 0·05 | 1·47 | 1·23 | <0·01 | 0·18 | 0·04 | 0·09 | 0·76 | 0·01 | 2·68 | 99·40 | 28·70 | 0·54 |
| DP8 | Bedded chert | 94·38 | 0·05 | 1·39 | 0·52 | <0·01 | 0·16 | 0·06 | 0·08 | 0·70 | 0·03 | 2·47 | 99·84 | 12·13 | 0·73 |
| TP20 | Bedded chert | 93·73 | 0·03 | 0·50 | 0·54 | <0·01 | 0·45 | 0·87 | 0·18 | 0·14 | 0·29 | 2·78 | 99·51 | 21·00 | 0·48 |
| TP39 | Bedded chert | 97·03 | 0·02 | 1·03 | 0·36 | <0·01 | 0·07 | 0·03 | 0·08 | 0·49 | 0·01 | 0·35 | 99·47 | 21·00 | 0·74 |
| TP42 | Bedded chert | 95·83 | <0·01 | 0·33 | 0·34 | <0·01 | 0·40 | 0·55 | 0·08 | 0·07 | 0·03 | 1·81 | 99·44 | 39·67 | 0·49 |
| Average values | | 94·65 | 0·05 | 1·34 | 0·72 | | | | | | | | | 20·71 | 0·63 |

*Total Fe, Al/(Al + Fe) – $Al_2O_3/(Al_2O_3 + Fe_2O_3)$

**Table 2.** Barium, rare earth element and Yttrium abundances (ppm) in the chert across the Ediacaran–Cambrian boundary succession, western Hunan in South China.

| Sample | Chert facies | Ba | La | Ce | Pr | Nd | Sm | Eu | Gd | Tb | Dy | Y | Ho | Er | Tm | Yb | Lu | ΣREE | Ce/Ce* | Eu/Eu* | Pr/Pr* | $La_n/Yb_n$ |
|---|---|---|---|---|---|---|---|---|---|---|---|---|---|---|---|---|---|---|---|---|---|---|
| GZP04 | Mounded chert | 245·4 | 0·93 | 1·17 | 0·15 | 0·47 | 0·10 | 0·05 | 0·08 | 0·02 | 0·11 | 0·48 | 0·02 | 0·08 | 0·01 | 0·08 | 0·01 | 3·75 | 0·72 | 2·64 | 1·16 | 0·81 |
| GZP04C | Mounded chert | 539·9 | 1·41 | 1·47 | 0·22 | 0·84 | 0·20 | 0·11 | 0·20 | 0·04 | 0·29 | 1·60 | 0·07 | 0·22 | 0·04 | 0·24 | 0·04 | 6·98 | 0·60 | 2·39 | 1·13 | 0·43 |
| GZP04CR | Mounded chert | 548·6 | 1·46 | 1·54 | 0·23 | 0·87 | 0·21 | 0·11 | 0·21 | 0·04 | 0·30 | 1·67 | 0·07 | 0·22 | 0·04 | 0·25 | 0·04 | 7·24 | 0·60 | 2·28 | 1·15 | 0·43 |
| GZP04E | Mounded chert | 802·1 | 0·80 | 1·01 | 0·14 | 0·53 | 0·12 | 0·29 | 0·15 | 0·03 | 0·16 | 1·45 | 0·03 | 0·10 | 0·01 | 0·10 | 0·02 | 4·93 | 0·69 | 11·07 | 1·12 | 0·59 |
| DP2 | Mounded chert | 16156·6 | 1·90 | 2·54 | 0·27 | 1·14 | 0·36 | 2·00 | 0·43 | 0·07 | 0·48 | 4·56 | 0·13 | 0·41 | 0·07 | 0·48 | 0·08 | 14·92 | 0·79 | 24·91 | 0·93 | 0·29 |
| Average values | | | | | | | | | | | | | | | | | | 7·56 | 0·68 | 8·66 | 1·10 | 0·51 |
| GZP26' | Vein chert | 472·6 | 2·02 | 2·66 | 0·29 | 1·02 | 0·27 | 0·10 | 0·17 | 0·04 | 0·26 | 1·06 | 0·06 | 0·18 | 0·03 | 0·18 | 0·03 | 8·36 | 0·78 | 1·91 | 1·04 | 0·83 |
| GZP29' | Vein chert | 473·9 | 5·67 | 6·34 | 0·89 | 2·72 | 0·54 | 0·16 | 0·40 | 0·07 | 0·53 | 2·86 | 0·13 | 0·40 | 0·07 | 0·44 | 0·07 | 21·28 | 0·64 | 1·50 | 1·27 | 0·95 |
| GZP30'W | Vein chert | 14·1 | 0·06 | 0·07 | 0·01 | 0·06 | 0·01 | 0·01 | 0·02 | 0·00 | 0·02 | 0·88 | 0·00 | 0·01 | 0·00 | 0·02 | 0·00 | 1·17 | 0·55 | 2·52 | 1·24 | 0·24 |
| Average values | | | | | | | | | | | | | | | | | | 10·27 | 0·66 | 1·97 | 1·18 | 0·67 |
| TP27 | Brecciated chert | 1832·0 | 2·74 | 3·32 | 0·56 | 1·81 | 0·31 | 0·20 | 0·31 | 0·05 | 0·28 | 2·28 | 0·06 | 0·22 | 0·04 | 0·30 | 0·05 | 12·54 | 0·62 | 3·17 | 1·33 | 0·67 |
| TP28 | Brecciated chert | 11614·8 | 2·72 | 2·80 | 0·46 | 1·44 | 0·23 | 0·90 | 0·25 | 0·04 | 0·24 | 2·16 | 0·05 | 0·17 | 0·03 | 0·20 | 0·04 | 11·73 | 0·57 | 18·86 | 1·33 | 1·00 |
| TP31 | Brecciated chert | 4210·9 | 4·03 | 3·10 | 1·03 | 4·43 | 1·01 | 0·15 | 1·16 | 0·21 | 1·43 | 12·74 | 0·32 | 0·95 | 0·15 | 0·90 | 0·13 | 31·72 | 0·35 | 0·66 | 1·38 | 0·33 |
| TP33 | Brecciated chert | 2095·5 | 0·74 | 0·65 | 0·18 | 0·90 | 0·25 | 0·20 | 0·38 | 0·07 | 0·46 | 4·26 | 0·11 | 0·33 | 0·05 | 0·34 | 0·06 | 8·98 | 0·41 | 3·25 | 1·18 | 0·16 |
| TP37 | Brecciated chert | 6553·5 | 1·47 | 2·11 | 0·47 | 2·35 | 0·69 | 0·56 | 0·72 | 0·11 | 0·58 | 3·43 | 0·11 | 0·26 | 0·03 | 0·21 | 0·03 | 13·13 | 0·58 | 4·05 | 1·12 | 0·51 |
| Average values | | | | | | | | | | | | | | | | | | 15·62 | 0·51 | 6·00 | 1·27 | 0·53 |
| GZP12' | Bedded chert | 3044·0 | 5·43 | 7·23 | 1·27 | 5·03 | 1·21 | 0·16 | 1·02 | 0·18 | 1·15 | 6·63 | 0·25 | 0·74 | 0·11 | 0·79 | 0·13 | 31·34 | 0·64 | 0·69 | 1·20 | 0·51 |
| GZP17' | Bedded chert | 1700·5 | 1·88 | 2·74 | 0·31 | 1·10 | 0·29 | 0·01 | 0·16 | 0·03 | 0·23 | 0·85 | 0·06 | 0·18 | 0·03 | 0·21 | 0·03 | 8·10 | 0·81 | 0·15 | 1·06 | 0·65 |
| GZP22' | Bedded chert | 916·1 | 2·02 | 2·80 | 0·36 | 1·34 | 0·33 | 0·15 | 0·15 | 0·03 | 0·19 | 0·44 | 0·05 | 0·15 | 0·03 | 0·19 | 0·03 | 8·24 | 0·75 | 2·73 | 1·10 | 0·79 |
| GZP24' | Bedded chert | 622·0 | 1·79 | 2·50 | 0·29 | 1·00 | 0·25 | 0·11 | 0·12 | 0·02 | 0·16 | 0·43 | 0·04 | 0·14 | 0·02 | 0·17 | 0·03 | 7·07 | 0·79 | 2·47 | 1·07 | 0·78 |
| GZP25' | Bedded chert | 688·0 | 2·78 | 3·58 | 0·39 | 1·26 | 0·29 | 0·12 | 0·16 | 0·04 | 0·28 | 1·25 | 0·07 | 0·23 | 0·04 | 0·27 | 0·04 | 10·80 | 0·77 | 2·22 | 1·06 | 0·76 |
| DP5 | Bedded chert | 793·2 | 2·83 | 3·07 | 0·57 | 1·94 | 0·48 | 0·17 | 0·52 | 0·09 | 0·67 | 5·26 | 0·17 | 0·54 | 0·09 | 0·63 | 0·11 | 17·12 | 0·56 | 1·58 | 1·35 | 0·33 |
| DP6B | Bedded chert | 681·1 | 1·73 | 2·20 | 0·29 | 1·21 | 0·30 | 0·23 | 0·36 | 0·07 | 0·44 | 3·26 | 0·10 | 0·33 | 0·05 | 0·37 | 0·06 | 11·00 | 0·71 | 3·25 | 1·04 | 0·35 |
| DP7 | Bedded chert | 745·4 | 0·72 | 0·88 | 0·10 | 0·42 | 0·11 | 0·23 | 0·19 | 0·03 | 0·23 | 2·34 | 0·06 | 0·24 | 0·04 | 0·30 | 0·05 | 5·93 | 0·72 | 7·82 | 0·99 | 0·18 |
| DP8 | Bedded chert | 791·4 | 0·84 | 1·47 | 0·18 | 0·70 | 0·20 | 0·11 | 0·15 | 0·03 | 0·26 | 2·07 | 0·07 | 0·23 | 0·04 | 0·29 | 0·05 | 6·68 | 0·86 | 2·62 | 1·07 | 0·22 |
| TP20 | Bedded chert | 8498·3 | 5·84 | 4·56 | 1·57 | 7·15 | 1·82 | 1·25 | 2·17 | 0·37 | 2·50 | 20·32 | 0·58 | 1·71 | 0·25 | 1·60 | 0·25 | 51·93 | 0·35 | 3·08 | 1·33 | 0·27 |
| TP39 | Bedded chert | 4563·1 | 1·33 | 0·73 | 0·29 | 0·93 | 0·18 | 0·03 | 0·16 | 0·03 | 0·24 | 2·20 | 0·06 | 0·19 | 0·03 | 0·22 | 0·04 | 6·66 | 0·27 | 0·70 | 1·78 | 0·44 |
| TP42 | Bedded chert | 4089·5 | 4·20 | 2·54 | 1·16 | 4·82 | 1·06 | 0·11 | 1·02 | 0·16 | 1·07 | 9·50 | 0·24 | 0·75 | 0·12 | 0·80 | 0·12 | 27·67 | 0·26 | 0·51 | 1·50 | 0·39 |
| Average values | | | | | | | | | | | | | | | | | | 16·05 | 0·62 | 2·32 | 1·21 | 0·47 |

for one low value due to a high $TFe_2O_3$ content derived from mounded chert. The $TFe_2O_3$ contents are relatively high (average 3·51%) in the mounded chert, and low in the brecciated chert (average 0·58%). The $Al_2O_3$ contents are relatively high in the vein (average 1·28%) and bedded chert (average 1·34%), and low in the mounded (average 0·95%) and brecciated chert (average 0·66%). The $TiO_2$ contents are persistently low among all four types of chert. Accordingly, the $Al_2O_3/(Al_2O_3 + Fe_2O_3)$ ratios are the lowest in the mounded chert (average 0·23), increasing from vein chert (average 0·31), to brecciated chert (average 0·48) and to bedded chert (average 0·63), respectively. The Fe/Ti ratios are the highest in the mounded chert (average 78·30), decreasing from vein chert (average 42·19), to brecciated chert (average 31·52) and to bedded chert (average 20·71). The Ba contents vary widely from 14·12 ppm (i.e. in vein chert), to 1·62% (i.e. in the mounded chert).

The shale PAAS-normalized REE patterns for the four types of chert are given in Fig. 6A to D. Generally, most of the samples exhibit apparent convex REE patterns, with intermediate negative Ce anomalies and intermediate to high positive Eu anomalies, particularly from the mounded chert, whereas a few samples from vein and bedded chert have slightly flat REE patterns with negative Eu anomalies. The total REE contents (ΣREE) are generally very low in all types of chert (<51·9 ppm), particularly in the mounded chert (average 7·56 ppm). The Ce/Ce* ratios vary from 0·60 to 0·79 (average 0·68) in the mounded chert, from 0·35 to 0·62 (average 0·51) in brecciated chert, from 0·55 to 0·78 (average 0·66) in the vein chert, and from 0·26 to 0·86 (average 0·62) in bedded chert, representing intermediate negative Ce anomalies in all types of chert. Eu/Eu* ratios are variable from 2·28 to 24·91 (average 8·66) in mounded chert, from 0·66 to 18·86 (average 6·00) in brecciated chert, from 1·50 to 2·52 (average 1·97) in vein chert, and from 0·15 to 7·82 (average 2·32) in bedded chert. More than half of the samples have ratios of Eu/Eu* larger than 1·50, which indicates apparently positive Eu anomalies. Except for two samples, Pr/Pr* ratios are larger than 1·05 in all types of chert, but less than 1·78 (average 1·20). The $La_n/Yb_n$ ratios are mostly less than 1·00 in the four lithological types except for two samples (GZP29' and TP28).

## INTERPRETATION AND DISCUSSION

### Petrological constraints on chert formation

*Mounded chert*

The presence of voids and/or channels lined by botryoidal chalcedony cements under domal chert units, and of relict vent spouts on the surface (Fig. 3B and D) suggests that these features were

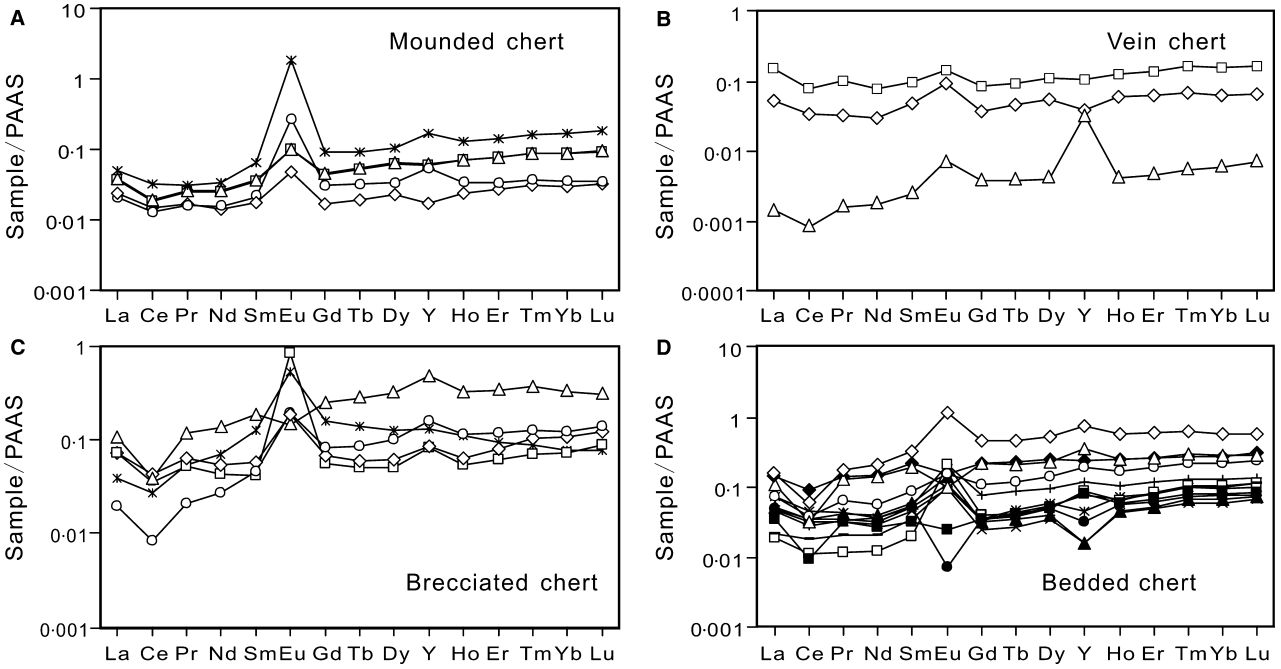


**Fig. 6.** PAAS-normalized REE abundance patterns of different types of chert (mounded, vein, brecciated and bedded chert). Most chert types show apparent positive Eu anomalies and weak to intermediate negative Ce anomalies.

 

formed along the fluid pathways generated through hydrothermal venting of silica-rich fluid migrating upward from depth. Alternative explanations that these were formed through silica permineralization or replacement of former carbonates were not accepted, as these structures apparently are not associated with the former carbonates (i.e. extensive microbial lamination in the absence of evaporites; Hesse, 1988). However, such emanating outlets were easily plugged and rarely preserved due to the nature of silica gel. The botryoidal (or spheroidal) and fibrous silica cements in voids and channels (Figs 3E, 4A and 4B) are also unlikely to have been a product of silica replacement, but rather a product precipitated from the rapidly cooling silica-rich fluid as a result of interactions between hydrothermal fluids and sea water (Herzig *et al.*, 1988; Stüben *et al.*, 1994; Hopkinson *et al.*, 1999). Chalcedony fibres are indicators of silica polymer chain linearity, a function of pH levels of fluids (Heaney, 1993), which is favoured in rapidly cooling acidic siliceous solutions due to widespread suppression of silica polymer cross-branching (Hopkinson *et al.*, 1999). On the other hand, as evidenced by the microthermometric data stated earlier, occurrences of minor, wall-lining granular microquartz and drusy macroquartz, as well as barite and pyrite crystals in voids and veins (Figs 3E, 4A and 4B), are probably a reflection of secondary mineral formation through secondary heating and recrystallization in a relatively silica-poor fluid at a higher temperature (Alt *et al.*, 1987; Stüben *et al.*, 1994). Therefore, the coexistence of amorphous silica, fibrous chalcedony, micro-macro quartz and barite, as well as pyrite in some cases, can be attributed to variable supersaturations and rates of nucleation and growth in response to episodic hydrothermal activities (Hopkinson *et al.*, 1999). Minor saddle dolomite cements along some voids and/or vent channels (Figs 3E and 4C) could have been precipitated from the early hydrothermal fluids, with Mg ions probably sourced from the underlying Neoproterozoic dolostones (i.e. Dengying and Doushantuo formations) through interactions of upwelling hydrothermal fluids with the host dolostones. The amorphous silica host (or matrix) and disseminated pyrite are indicative of precipitation under a combination of conductive cooling, together with intermixing of hydrothermal fluids with sea waters at low-temperature (*ca* 50°C) diffusive vent fields as observed on the modern oceanic sea floor (Herzig *et al.*, 1988; Stüben *et al.*, 1994; Halbach *et al.*, 2002).

Rare minerals, such as sanidine and muscovite in chert, are unlikely to be products of the silica replacement of carbonates or to occur through direct precipitation from normal sea water. A more likely mechanism of introducing these minerals would be through the addition of tuffaceous admixture; on the other hand, their presence may account for the slight increase in $Al_2O_3$ contents as described earlier, compared with those of reported silica chimneys on oceanic ridges (Herzig *et al.*, 1988; Stüben *et al.*, 1994). Additionally, Fe-sulphides (or their alteration products) and barites are common smoker minerals (Herzig *et al.*, 1988; Stüben *et al.*, 1994; Halbach *et al.*, 2002); their presence in the mounded chert would also reconcile hydrothermal venting as the mechanism responsible for their formation. Thus, minor void or vein-filling barites (Figs 3F and 4B) probably were precipitated from upflow Ba-rich vent fluids upon mixing of relatively sulphate-rich sea waters with respect to hydrothermal fluids (Bertine & Keene, 1975; Stüben *et al.*, 1994; Halbach *et al.*, 2002). This scenario is supported by $^{34}S$-depleted sulphate sulphur isotopic data (18·8‰ VCDT) compared with that of coeval sea water sulphate (*ca* 35‰ VCDT) (Chen *et al.*, 2009), and microthermometric data as listed earlier. On the Yangtze Platform, abundant barite and witherite deposits occur in the lowermost Cambrian black shale successions both along the northern and southern marginal zones (Fig. 1A). These deposits were proposed to have been precipitated from Ba-rich hydrothermal (or volcanic-derived) fluids (Xia *et al.*, 2004) or, alternatively, upon mixing with anoxic sulphate-bearing sea waters (Wang & Li, 1991; Wang & Chu, 1993). In addition, the Fe-oxyhydroxide shrubs preserved in the silica matrix may represent the silicified remains of microbial filaments (Duhig *et al.*, 1992); if so, the extremophilic microbes could have colonized extensively in the silica vents, as is seen widely in modern and ancient hydrothermal vent systems (Humphris *et al.*, 1995; Jones & Renaut, 2003; Lowe & Braunstein, 2003; Van Kranendonk, 2006). The presence of volcanic glass shards in the mounded chert units (Fig. 4E), however, excludes silica replacement as the mechanism responsible for their formation and suggests concurrent volcanic activities in neighbouring regions.

### *Vein chert*

The vein chert, occurring as vein infills, was probably precipitated along the fracture/vein systems as a result of cooling of the silica-rich

 

hydrothermal fluids when they flowed upward, particularly as they flowed into the distal branches away from the main fractures. The minor quartz cements probably reflect occasional secondary heating and/or recrystallization at higher temperature, liquid-deficient episodes, such as those void/vesicle-filled quartz crystals seen in mounded chert as documented above. Its termination below the mounded or bedded chert units (Fig. 2), thus, further supports that silica-rich hydrothermal fluids from the deep-seated hydrothermal sources were channelled through the fault and/or fracture conduits.

*Brecciated chert*

The splayed or funnel-shaped brecciated chert 'intrusions' that cross-cut the uppermost dolostone horizon (Figs 2 and 4G) were probably formed by more intensive fracturing or overpressure hydrofracturing, thereby cross-cutting the uppermost dolostones. In this case, intense brecciation could have taken place along the fracture zone, along which the angular breccias were then silicified by ascending silica-rich hydrothermal fluids; simultaneously minor silica and secondary dolomite precipitated along the fractures. Compared with the vein chert, this facies was probably formed along larger-scale fracture conduits induced by more intense fracturing. This brecciated chert, in association with vein chert as described above is, to some extent, similar to the Archaean chert in the Pilbara Supergroup, Western Australia, where chert breccia and chert ± barite ± Fe veins, occurred as the hydrothermal fluid pathways that linked the deep magma chambers to the overlying bedded chert units (Nijman *et al.*, 1998; Van Kranendonk, 2006).

*Bedded chert*

The stratified chert beds reflect cyclic variations of silica flux during deposition, thus thin-bedded chert, with respect to the thick-bedded counterpart, indicates deposition with a low silica flux (or low depositional rate). The horizontal fine lamination, commonly developed in thin-bedded chert, further suggests a relatively quiet and deep setting where weak current agitation favoured formation and preservation of lamination, reconciling a lower depositional rate as well. On the marginal zone, the thickness of the chert beds can, therefore, to some extent, reflect the distance to the vent fields; the shorter the distance the thicker the bed thickness (or the higher silica flux and depositional rate) and *vice versa*. Compared with the relatively high relief and agitation of exhalative fluids around the vent centre, a relatively quiet and deep pool would also favour the preservation of tuffaceous fallouts, as observed in this case. However, it is unlikely that so few layers of thin tuffs, generally 1 to 3 cm thick, could provide enough silica for the widespread deposition of chert up to a hundred metres thick across the E–C boundary successions. The worm-like biotic remains (Fig. 4H), resembling *Palaeopascichnus jiumenensis* described by Dong *et al.* (2008), may represent a specific species adapted to the conditions around hydrothermal vent fields, as seen near modern hydrothermal vents. The absence of silica-accreting biota (i.e. sponges) in the chert suggests that biogenic precipitation of silica was not a major contribution to chert formation, at least in the study area.

## Constraints from microthermometry of fluid inclusions

Microthermometric data (Fig. 5) indicate that the void/vein-lining quartz and barite crystals in the chert (except for the bedded chert) were precipitated in hydrothermal brine fluids at temperatures of at least 120°C (up to 177°C) within emanating channels, although it may be variable from place to place. The high salinity of primary fluids (*ca* five to seven times sea water salinity) indicates that the phase separation of magmatic or sea water-derived fluids must have occurred at higher temperatures at depth (Bodnar *et al.*, 1985; Bischoff & Pitzer, 1989; Tivey *et al.*, 1998). The absence of fluid inclusions in the botryoidal chalcedony, however, attests to a low-temperature fluid being responsible for their precipitation; an even lower temperature is commonly considered to be responsible for the precipitation of amorphous silica (Herzig *et al.*, 1988; Halbach *et al.*, 2002). This observation indicates that the temperature of venting fluids in the same vent fields could be variable at different vents or venting episodes. The hydrothermal fluids at depth, however, should be higher in temperature, and were subject to rapid conductive cooling and mixing with the cool sea water during the course of upward migration, leading to substantial precipitation of amorphous silica at a lower temperature on the sea floor. Lott *et al.* (1999) identified hydrothermal quartz veins, yielding homogenization temperatures of primary fluid inclusions up to 290°C, in the dolostones about 10 m below the boundary between Niutitang (black shales) and Dengying formations in western Hunan, generally in agreement with the data presented in this paper.

## Constraints from element geochemistry

In marine basins, siliceous sediments can deposit either from normal marine waters or from hydrothermal fluids. High concentrations of silica and iron in sediments are typical of hydrothermal discharges on the sea floor as a result of fluid–rock interactions (Herzig *et al.*, 1988; Stüben *et al.*, 1994; Halbach *et al.*, 2002). In this study, the Liuchapo chert deposits generally have $SiO_2$ concentrations >92 wt%, indicating a fairly high influx of silica into the ocean. The Fe influx is commonly assessed by the $Al_2O_3/(Al_2O_3 + Fe_2O_3)$ ratio (Murray, 1994) and/or the Fe/Ti ratio (Boström, 1983) of siliceous sediments; low $Al_2O_3/(Al_2O_3 + Fe_2O_3)$ ratios or high Fe/Ti ratios point to a high Fe influx. The low $Al_2O_3/(Al_2O_3 + Fe_2O_3)$ ratios of mounded, brecciated and vein chert, compared with those of bedded chert, indicate higher Fe influxes, thereby implying stronger hydrothermal influences when they precipitated with respect to the bedded chert. Some authors (Boström, 1983) suggested that hydrothermal-originated chert deposits generally yield Fe/Ti ratios ≥20. The chert samples in this study mostly have Fe/Ti ratios ≥20, especially those derived from the mounded chert (Table 1), pointing to precipitation apparently influenced by hydrothermal activity. The lower $Al_2O_3$ contents (Table 1; Fig. 7A) indicate that the chert was unlikely to have formed from the alteration of volcanic or volcaniclastic rocks commonly yielding high $Al_2O_3$ concentrations contributed by aluminosilicate minerals; this is consistent with the rare presence of tuffaceous layers in the chert successions. High Ba contents in some chert beds are probably a reflection of the high abundance of barite, reconciling a hydrothermal origin in view of the high Ba associated with hydrothermal fluids (Bertine & Keene, 1975; Stüben *et al.*, 1994; Halbach *et al.*, 2002).

In the sea floor hydrothermal system, REE patterns of vent fluids generally show an apparent enrichment in LREEs relative to HREEs with pronounced positive Eu anomalies and weak or no negative Ce anomalies (Michard *et al.*, 1983; German *et al.*, 1990, 1999), as a result of crystochemical exchange with plagioclase phenocrysts formed in the vent and speciation of vent fluids (Douville *et al.*, 1999). Therefore, sediments deposited from vent fluids generally inherit the REE patterns of the parent vent fluids, i.e. with

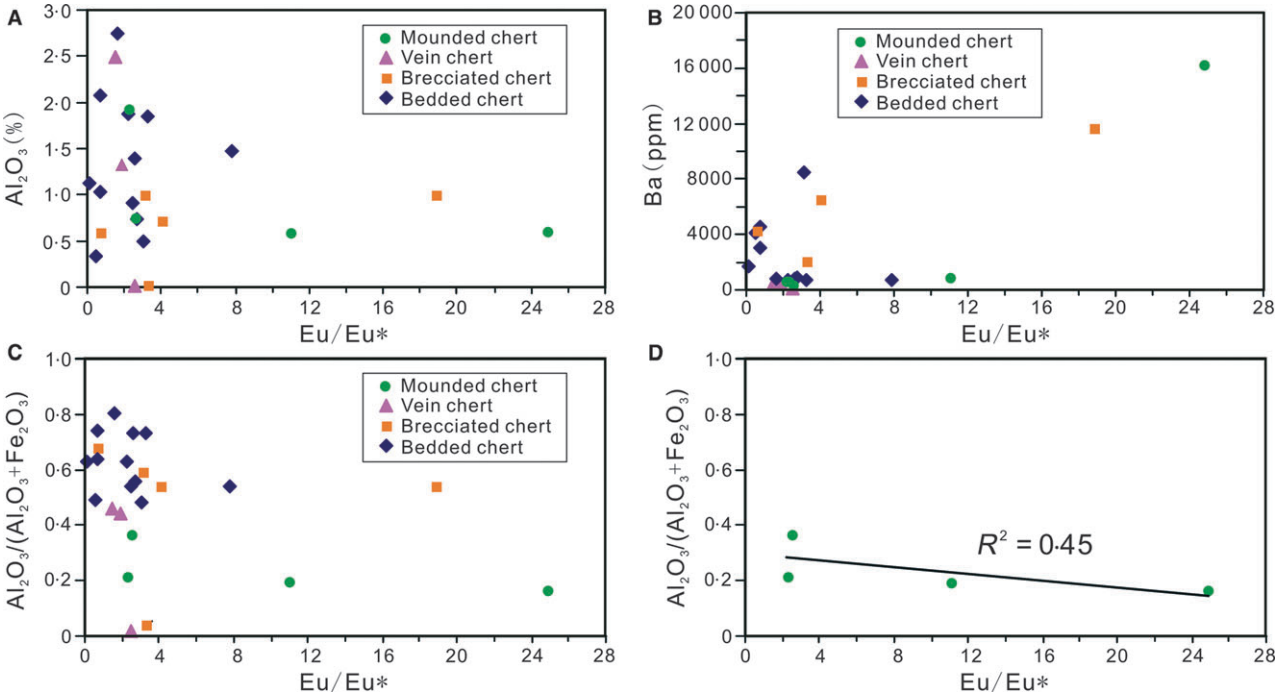


**Fig. 7.** (A) Cross-plots of Eu/Eu* and $Al_2O_3$ contents (wt%) in different types of chert, no linear relationship is present between them. (B) Cross-plots of Eu/Eu* and Ba content (ppm) in different types of chert; although correlation between them exists, it becomes weak if the two samples with high Ba contents are excluded. (C) Cross-plots of Eu/Eu* and $Al_2O_3/(Al_2O_3 + Fe_2O_3)$ ratios in different types of chert where correlation is weak. (D) Cross-plots of Eu/Eu* and $Al_2O_3/(Al_2O_3 + Fe_2O_3)$ ratios in the mounded chert. Note the lowest $Al_2O_3/(Al_2O_3 + Fe_2O_3)$ ratios and enhanced negative correlation ($R^2 = 0.45$).

 

positive Eu anomalies (German *et al.*, 1990; Mills & Elderfield, 1995), although REE patterns will vary as the influx of ambient sea water increases. Most of the samples in this study, except for a few samples of bedded chert, display positive Eu anomalies (Fig. 6A to D), particularly for the mounded chert, suggesting a strong influence of hydrothermal fluids on their precipitation (Douville *et al.*, 1999). Although detrital feldspar minerals can also lead to the positive Eu anomalies (Owen *et al.*, 1999), the absence of correlation of Eu anomalies with $Al_2O_3$ contents (Fig. 7A) indicates that aluminosilicate minerals, such as feldspar, did not contribute to the positive Eu anomalies (Kato & Nakamura, 2003).

Previous studies showed that positive Eu anomalies may result from various Ba-compound interferences during analysis (Dulski, 1994). The method to calculate the Eu anomalies proposed by Dulski (1994) is supposed to decrease such effects resulting from the analytical process. Although covariance is revealed between the ratios of Eu/Eu* and Ba contents, this relationship tends to be weak if excluding the two samples (DP2 and TP28) with high Ba contents (Fig. 7B). Thus, the high ratios of Eu/Eu* in the two samples probably are influenced in part by Ba interference. By comparison, such effects on the rest of the samples are relatively weak. In addition, high Ba contents in silica deposits are a common characteristic of hydrothermal products (Stüben *et al.*, 1994; Urabe & Kusakabe, 1990). Although the negative correlation between $Al_2O_3/(Al_2O_3 + Fe_2O_3)$ and Eu/Eu* ratios is generally weak for all types of chert (Fig. 7C), it is enhanced in mounded chert (Fig. 7D), implying that the positive Eu anomalies were positively associated with increased Fe flux which, in turn, was enhanced by hydrothermal activity during deposition (Murray, 1994). The relatively low magnitude of positive Eu anomalies in vein chert suggests that this type of chert might have precipitated from the waning hydrothermal fluids near the end of hydrothermal activity and/or in the distal parts of fracture systems away from the principal conduit zone. The presence of negative Eu anomalies in a few samples of bedded chert, on the other hand, suggests precipitation in a sea water-dominant fluid away from the hydrothermal vent centre.

The REE patterns of sea water are characterized by depletion in LREEs relative to the HREEs with apparent negative Ce anomalies and no Eu anomalies (Elderfield & Greaves, 1982). Thus, mixing of sea water with hydrothermal fluids will produce hybrid REE patterns inherited from the two primary fluids, as indicated by relative depletion in LREEs with both negative Ce and positive Eu anomalies. The extent to which this occurs depends on the fractions between the two primary fluids involved (Mills & Elderfield, 1995). Most of the studied samples yield Pr/Pr* ratios >1·05, indicating that the negative Ce anomalies are authentic, rather than a result of La enrichment (Bau & Duski, 1996). The flat REE patterns with, more or less, negative Ce anomalies for most of the chert samples (Fig. 6A to D) indicate that their formation involved both sea water and hydrothermal fluid, rather than just the latter. A similar situation is seen in other examples of modern and ancient ocean hydrothermal systems (German *et al.*, 1990, 1999; Mills & Elderfield, 1995; Kato & Nakamura, 2003; Chen *et al.*, 2006). Therefore, the highest degree of positive Eu anomalies accompanying weak to no negative Ce anomalies in mounded and brecciated chert points towards precipitation under the strongest hydrothermal conditions when compared with the other types of chert facies. Most samples demonstrate positive, but very weak, Y distribution patterns, suggesting, more or less, mixing between hydrothermal fluid and sea water during their deposition (Bau & Duski, 1996; Douville *et al.*, 1999). The REE geochemical data fully support the scenario revealed by petrological and microthermometric data as documented above.

## Depositional setting

On the modern oceanic sea floor, the occurrence of amorphous silica in association with sulphides and/or sulphates is quite common in hydrothermal systems. Herzig *et al.* (1988) reported inactive silica chimneys in the rift valley of the Galapagos spreading centre at depth of 2600 m ('Cauliflower Garden'). These silica chimneys were formed at temperatures between 32°C and 42°C; they consist of mainly porous and cell-like, soft silica, spongy or honeycomb-like in appearance with abundant cavities and vesicles, and locally are associated with minor sulphide and Mn-Fe oxyhydroxides. Numerous sub-concentric tube-like structures may represent small vent conduits. A hydrothermal silica chimney field was also found in the median rift valley of the Mariana Trough backarc spreading centre ('Topless Tower'; Stüben *et al.*, 1994), where the chimneys are characterized by an irregular surface and consist almost entirely of amorphous silica and barite. The silica-rich parts are spongy in appearance, and

contain abundant cavities and voids, which locally are infilled by cryptocrystalline, chalcedony-like aggregates. Hypidiomorphous pyrite crystals are disseminated throughout the amorphous silica along the fluid channels. These crystals suggest that silica chimneys mainly occurred at temperatures between 41°C and 50°C, although a higher temperature (about 230°C) may have occurred in the inner part where pyrite, barite, marcasite and quartz were formed along the fluid channels. Halbach *et al.* (2002) first reported sulphide-impregnated and pure silica precipitates of hydrothermal origin from the central Indian Ocean, where jasper occurs without columnar and/or zonal structures, or associated feeder channels. Smaller cracks or voids within the jasper horizon commonly were plugged by sulphide minerals formed during hydrothermal infiltration; the remaining larger cavities often are lined with ZnS, FeS and/or $BaSO_4$ crystals. These iron-rich silica deposits were precipitated from a low-temperature (about 60°C) diffusive vent fluid, and sphalerite and barite-impregnations were precipitated from a fluid at intermediate temperatures between 155°C and 265°C, based on fluid inclusion data.

Textural and compositional similarities with silica chimneys on the modern oceanic sea floor (Herzig *et al.*, 1988; Stüben *et al.*, 1994; Halbach *et al.*, 2002) and older examples (Nijman *et al.*, 1998; Van Kranendonk, 2006) as described above, make it reasonable to assume that the Liuchapo chert deposits, especially those mounded and associated vein/splayed brecciated chert bodies along the carbonate platform margin, were precipitated in submarine silica-rich hydrothermal vent fields (Fig. 8). Similar textures and compositions, however, also occur in silica deposits forming in subaerial siliceous hot springs (geysers; Jones & Renaut, 2003; Lowe & Braunstein, 2003).

The occurrences of dolostone breccias on the foreslope underlying the chert wedge, i.e. at Tianping (Fig. 2) and subaerial exposure (karstic) unconformities in the upper part of Dengying Formation toward the platform margin and interior (Xue *et al.*, 1992), probably resulted from block-tilting, in the context of basin rifting on the Yangtze Block (Wang & Li, 2003), as reflected by the isolated carbonate platform-basin configuration (Fig. 1A). The sharp lateral contact between carbonates and the chert deposits, and vertical facies offset across the marginal zone (Fig. 2) further reconciles syndepositional extensional faulting at depth under the platform margin. It was the syndepositional faulting that produced a terraced sea floor across the margin and provided conduits for silica-rich fluids to migrate upward from depth, forming silica chimney fields on the sea floor (Fig. 8). A small portion of this silica could have precipitated directly from the fluids to form the mounded chert around silica chimneys (or vents) and vein/brecciated chert along the fractured conduits as a result of

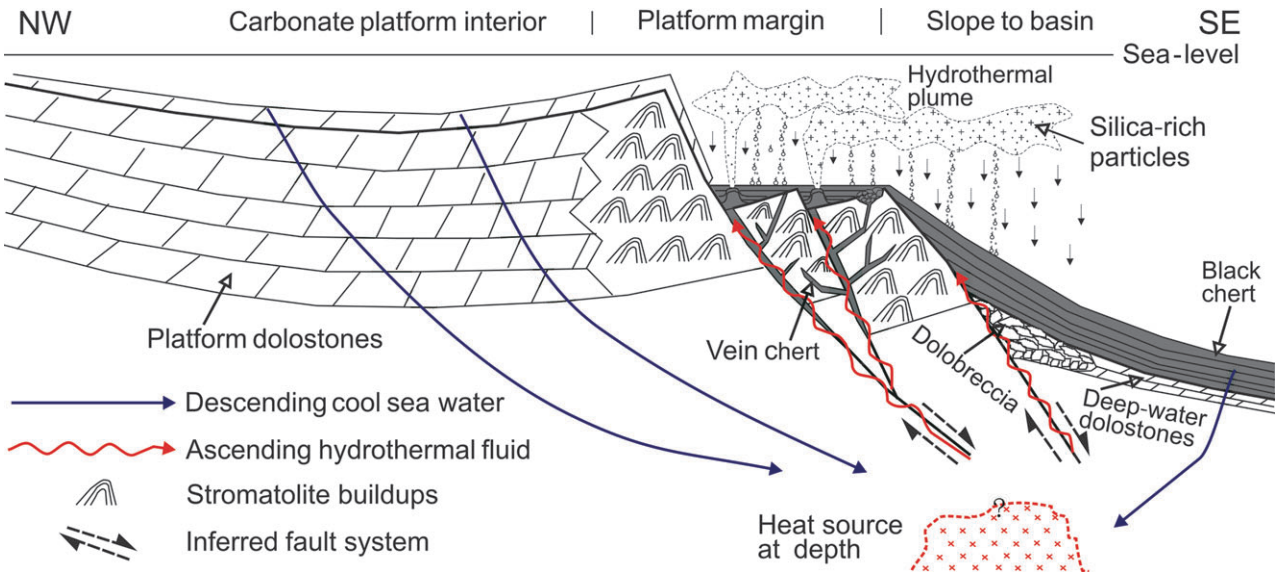


**Fig. 8.** Conceptual model showing the tectono-depositional setting for the development of hydrothermal venting fields and chert deposition on the terraced margin of the Yangtze Platform and further basinward, South China during the Ediacaran–Cambrian transition.

 

conductive cooling and mixing with cooling sea water (Herzig *et al.*, 1988; Stüben *et al.*, 1994). However, most of the silica-rich hydrothermal fluids were vented into the water column, generating hydrothermal plumes that moved away from the vents, and simultaneously fell out onto the sea floor (Fig. 8). Initially thick-bedded, chert deposits thinned basinward away from the vent fields (Fig. 2) as hydrothermal influences waned and oceanic influences dominated. This scenario is further corroborated by fluid inclusion microthermometry and element geochemistry data as documented earlier.

Unlike the hydrothermal-originated chert directly fed by the volcanic chamber on the oceanic spreading centres (Herzig *et al.*, 1988; Stüben *et al.*, 1994; Halbach *et al.*, 2002), the chert deposits described here were not fed by a magma chamber immediately underneath. Instead, these chert deposits were precipitated from the hydrothermal fluids infiltrated through thick metasedimentary and sedimentary siliciclastic infills in the rift basin, resulting in minor differences particularly in their composition, i.e. relatively high Al contents. Such hydrothermal chert deposits along carbonate platform margins are rare, especially in the Phanerozoic. In view of the extensional tectonism on the Yangtze Block during the E–C transition, it is reasonable to suppose that lower-temperature hydrothermal activities, probably by diffusive venting or bubbling, may also have taken place on the basin floor, resulting in extremely silica-rich sea water, as indicated by widespread occurrences of bedded chert deposits off platform margins and further basinward. This observation can be analogous to the case in the modern Red Sea where the deep silica-rich hot (up to *ca* 67°C) brine pools in sub-basins were fed by hydrothermal activities, although vent fields have not been discovered on the sea floor (Schoell & Hartmann, 1978; Monin *et al.*, 1981; Cember, 1996; Winckler *et al.*, 2001).

Identification of hydrothermal silica chimneys in the E–C successions provides a unique line of evidence linked to the abnormal silica enrichment off the carbonate platform of the Yangtze Block during the E–C transition. The silica chimney systems occur mainly at three intervals (I to III); with the exception of the basal interval that sits locally on the Dengying dolostones (I), the other two intervals (II and III) generally comprise a basal, thin-bedded chert, followed by a middle vein and/or splayed brecciated chert body terminating under mounded and/or bedded chert horizons (Fig. 2). The enhanced hydrothermal activity was inherently a reflection of intensified tectonism; multiple episodes (I to III) of hydrothermal venting (Fig. 2) thus indicate episodic tectonic activity. The multiple occurrences of slumps and/or slides at the outer edge of the chert wedge, i.e. at Tianping and Siduping (Fig. 2) indicate that episodic slope failures may have taken place on the upper slope, implicating a temporal link to the structurally controlled hydrothermal activity as well. In view of the width of the vent field across the margin (*ca* 20 km) and the total length of the platform margin on the Yangtze Block (*ca* 5000 km), including the lost margin to the west (see Fig. 1), the vent fields along the margin are conservatively estimated to occupy an area of *ca* $10 \times 10^4$ km$^2$, assuming that vents were present on all platform margins. If the diffusive vents within the basin are included within this estimate, the area of the vent fields would be considerably larger. Under these circumstances, hydrothermal venting during the E–C transition could have influenced the oceanic environment and chemistry. The widespread chert deposits on the Yangtze Block alone are obviously a direct reflection of an extremely silica-rich ocean apparently different from that in the earlier Doushantuo and later Niutitang times. The temporal coincidences of the silica chimney occurrences with apparent geochemical perturbations (i.e. coupled negative C-S isotopic anomalies; Chen *et al.*, 2009), on the other hand, also support the conclusion that hydrothermal venting had induced fundamental changes in oceanic environment and chemistry through the release of vast amounts of reducing metal-rich fluids and gases (for example, $^{13}$C-depleted $CO_2$, $CH_4$ and $^{34}$S-depleted $H_2S$, $SO_2$) into the ocean and atmosphere (Corliss *et al.*, 1979; Herzig *et al.*, 1988; Halbach *et al.*, 2002; Resing *et al.*, 2004).

## CONCLUSIONS

Four lithotypes of chert in the Ediacaran–Cambrian (E–C) boundary successions along the margin of the Yangtze carbonate platform are distinguished, they are: mounded, vein, brecciated and bedded chert facies. The mounded chert units containing abundant primary voids and vesicles were formed at or near the vent fields, probably by both conductive cooling and intermixing of hydrothermal fluids with cool sea water. Vein chert was precipitated from ascending silica-rich hydrothermal fluids along the fractures. Splayed brecciated chert bodies were

formed in larger-scale fracture systems, probably by brecciation or overpressure hydrofracturing and simultaneous silicification and silica precipitation. The thin to medium-bedded chert horizons were precipitated in quiet water away from the vent fields from the silica-rich fallouts of hydrothermal plumes.

Although most of the chert deposits were formed in a low-temperature (<60°C) hydrothermal vent system, higher-temperature episodes (generally 120 to 180°C) of venting could have also occurred within vent centres or venting conduits. Most of the chert types are relatively rich in iron and show positive Eu anomalies in rare earth element distribution patterns, indicating an association with hydrothermal venting activities when precipitated.

The hydrothermal venting activity associated with thermal anomalies at depth occurred on the carbonate platform margin following the antecedent collage zone where deep-seated fault zones probably reactivated and acted as the feeders, allowing the hydrothermal fluids to move upward and emanate onto the sea floor to form silica chimneys, thereby resulting in precipitation of different types of chert across the margin and further basinward. This example provides a new insight into understanding the remarkable tectono-depositional and oceanic changes in this region, and elsewhere, during the E–C transition.

## ACKNOWLEDGEMENTS

This research was supported by the NSFC (Grant No. 40839907) and by the National Key Basic Research Program Project (973 Project) through grant 2005CB422101. We thank two anonymous reviewers for their critical comments, which were very helpful to improve the manuscript. Thanks also go to Associate Editor A. Immenhauser and Chief Editor P.K. Swart for their editorial help and comments.

## REFERENCES

**Alt, J.C., Lonsdale, P., Haymon, R.** and **Muehlenbachs, K.** (1987) Hydrothermal sulfide and oxide deposits on seamounts near 21°N, East Pacific Rise. *Geol. Soc. Am. Bull.*, **98,** 157–168.

**Amthor, J.E., Grotzinger, J.P., Schröder, S., Bowring, S.A., Ramezani, J., Martin, M.W.** and **Matter, A.** (2003) Extinction of *Cloudina* and *Namacalathus* at the Precambrian–Cambrian boundary in Oman. *Geology*, **31,** 431–434.

**Bau, M.** and **Duski, P.** (1996) Distribution of yttrium and rare-earth elements in the Penge and Kuruman iron-formations, Transvaal Supergroup, South Africa. *Precambrian Res.*, **79,** 37–55.

**Bertine, K.K.** and **Keene, J.B.** (1975) Submarine barite-opal rocks of hydrothermal origin. *Science*, **188,** 150–152.

**Bischoff, J.L.** and **Pitzer, K.S.** (1989) Liquid-vapor relations for the system NaCl-$H_2O$: summary of the P-T-x surface from 300 °C to 500 °C. *Am. J. Sci.*, **289,** 217–248.

**Bodnar, R.J.** (1993) Revised equation and table for determining the freezing point depression of $H_2O$-NaCl solutions. *Geochim. Cosmochim. Acta*, **57,** 683–684.

**Bodnar, R.J., Burnham, C.W.** and **Stern, S.M.** (1985) Synthetic fluid inclusions in natural quartz, III. Determinations of phase equilibrium properties in the system H2O-NaCl to 1000 °C and 1500 bars. *Geochim. Cosmochim. Acta*, **49,** 1861–1873.

**Boström, K.** (1983) Genesis of ferromanganese deposits – diagnostic criteria for recent and old deposits. In: *Hydrothermal Processes at Seafloor Spreading Centers* (Eds P.A. Rona, K. Boström, L. Laubier and K.L. Smith), pp. 473–483. Plenum Press, New York.

**Brasier, M.D.** (1995) The basal Cambrian transition and Cambrian bio-events (from terminal Proterozoic extinctions to Cambrian biomeres). In: *Global Events and Event Stratigraphy in the Phanerozoic* (Ed. O.H. Walliser), pp. 113–138. Spring-Verlag, Berlin.

**Cember, R.P.** (1996) Are undiscovered hydrothermal vents in the southern Red Sea the main source of silica and helium 3 for the Red Sea Deep Water? *J. Geophys. Res.*, **101,** 1225–1232.

**Chen, D.Z., Qing, H.R., Yan, X.** and **Li, H.** (2006) Hydrothermal venting and basin evolution (Devonian, South China): constraints from rare earth element geochemistry of chert. *Sed. Geol.*, **183,** 203–219.

**Chen, D.Z., Wang, J.G., Qing, H.R., Yan, D.T.** and **Li, R.W.** (2009) Hydrothermal venting activities in the Early Cambrian, South China: Petrological, geochrological and stable isotopic constraints. *Chem. Geol.*, **258,** 168–181.

**Corliss, J.B., Dymond, J., Forgon, L.I., Demond, J.M., von Herzen, R.P., Barllard, R.D., Green, K., Williams, D., Bainbridge, A., Grane, K.** and **Van Andel, T.H.** (1979) Submarin thermal springs on the Galapagos rift. *Science*, **203,** 1073–1083.

**Dong, L., Xiao, S., Shen, B.** and **Zhou, C.** (2008) Silicified *Horodyskia* and *Palaeopascichnus* from upper Ediacaran cherts in South China: tentative phlogenetic interpretation and implications for evolutionary stasis. *J. Geol. Soc. London*, **165,** 367–378.

**Douville, E., Bienvenu, P., Charlou, J.L., Donval, J.P., Fouquet, Y., Appriou, P.** and **Gamo, T.** (1999) Yttrium and rare earth elements in fluids from various deep-sea hydrothermal systems. *Geochim.Cosmochim. Acta*, **63,** 627–643.

**Duhig, N.C., Davidson, G.J.** and **Stolz, J.** (1992) Microbial involvement in the formation of Cambrian sea-floor silica-iron oxide deposits. *Geology*, **20,** 511–514.

**Dulski, P.** (1994) Interferences of oxide, hydroxide and chloride analyte species in the determination of rare earth elements in geological samples by inductively coupled plasma-mass spectrometry. *Fresen. Z. Anal. Chem.* **350,** 194–203.

**Elderfield, H.** and **Greaves, M.J.** (1982) The rare earth elements in seawater. *Nature*, **296,** 214–219.

**German, C.R., Klinkhammer, G.P., Edmond, J.M., Mitra, A.** and **Elderfield, H.** (1990) Hydrothermal scavenging of rare earth elements in the ocean. *Nature*, **345,** 516–518.

**German, C.R., Hergt, J., Palmer, M.R.** and **Edmond, J.M.** (1999) Geochemistry of a hydrothermal sediment core from the OBS vent field, 21°N East Pacific Rise. *Chem. Geol.*, **155,** 65–75.

**Goldberg, T., Poulton, S.W.** and **Strauss, H.** (2005) Sulfur and oxygen isotope signatures of late Neoproterozoic to early Cambrian sulphates, Yangtze Platform, China: diagenetic constraints and seawater evolution. *Precambrian Res.*, **137,** 223–241.

**Goldstein, R.H.** and **Reynolds, T.J.** (1994) Systematics of fluid inclusions and diagenetic minerals. *SEPM Short Course*, **31,** 1–199.

**Grotzinger, J.P., Bowring, B.Z., Saylor, B.Z.** and **Kaufman, A.J.** (1995) Biostratigraphic and geochronologic constraints on early animal evolution. *Science*, **270,** 598–604.

**Guo, Q.J., Shields, G.A., Liu, C.Q., Strauss, H., Zhu, M.Y., Pi, D.H., Goldberg, T.** and **Yang, X.L.** (2007) Trace element chemostratigraphy of two Ediacaran-Cambrian successions in South China: implications for organosedimentary metal enrichment and silicification in the early Cambrian. *Palaeogeogr. Palaeoclimatol. Palaeoecol.*, **254,** 194–216.

**Halbach, M., Halbach, P.** and **Lüders, V.** (2002) Sulfide-impregnated and pure silica precipitates of hydrothermal origin from the Central Indian Ocean. *Chem. Geol.*, **182,** 357–375.

**Heaney, P.J.** (1993) A proposed mechanism for the growth of chalcedony. *Contrib. Mineral. Petrol.*, **115,** 66–74.

**Herzig, P.M., Becker, K.P., Stoffers, P., Bäcker, H.** and **Blum, N.** (1988) Hydrothermal silica chimney fields in the Galapagos Spreading Center at 86°W. *Earth Planet. Sci. Lett.*, **89,** 261–272.

**Hesse, R.** (1988) Silica diagenesis: origin of inorganic and replacement cherts. *Earth-Sci. Rev.*, **26,** 253–284.

**Hopkinson, L., Roberts, S., Herrington, R.** and **Wilkinson, J.** (1999) The nature of crystalline silica from the TAG submarine hydrothermal mound, 26°N Mid Atlantic Ridge. *Contrib. Mineral. Petrol.*, **137,** 342–350.

**Humphris, S.E., Zierenberg, R.A., Mullineax, L.S.** and **Thomson, R.E.** (1995) Seafloor hydrothermal systems: physical, chemical, biological, and geological interactions. *AGU Geophys. Monogr.*, **91,** 466.

**Jiang, Y.H.** and **Li, S.Y.** (2005) A study of the fluid environment of silicalite transitional Precambrian-Cambrian age in Hunan and Guizhou Provinces. *Earth Sci. Frontier.*, **12,** 622–629 (in Chinese with English abstract).

**Jiang, G.Q., Shi, X.Y., Zhang, S.H., Wang, Y.** and **Xiao, S.H.** (2011) Stratigraphy and paleogeography of the Ediacaran Doushantuo Formation (ca. 635–551 Ma) in South China. *Gondwana Res.*, **19,** 831–849.

**Jones, B.** and **Renaut, W.** (2003) Petrography and genesis of spicular and columnar geyserite from the Whakarewarewa and Orakeikoraka geothermal areas, North Island, New Zealand. *Can. J. Earth Sci.*, **40,** 1585–1610.

**Kato, Y.** and **Nakamura, K.** (2003) Origin and global tectonic significance of Early Archean cherts from the Marble Bar greenstone belt, Pilbara Craton, Western Australia. *Precambrian Res.*, **125,** 191–243.

**Kimura, H.** and **Watanabe, Y.** (2001) Oceanic anoxia at the Precambrian-Cambrian boundary. *Geology*, **29,** 995–998.

**Li, Y.Y.** (1997) The geological characteristics of seafloor exhalative sedimentary chert in the Lower Cambrian-black shales in Dayong-Cili area, Hunan Province. *Acta Petrol. Sinica*, **13,** 121–126 (in Chinese with English abstract).

**Li, X.-H.** (1999) U-Pb zircon ages of granites from the southern margin of the Yangtze Block: timing of Neoproterozoic Jinning Orogeny in SE China and implication for Rodinian assembly. *Precambrian Res.*, **97,** 45–57.

**Li, S.R.** and **Gao, Z.M.** (1996) Silicalite of hydrothermal origin in the Lower Cambrian black rock series of South China. *Acta Miner. Sin.*, **16,** 416–422 (in Chinese with English abstract).

**Lott, D.A., Coveney, R.M.J.R., Murowichick, J.B.** and **Grauch, R.I.** (1999) Sedimentary exhalative nickel-molybdenum ores in south China. *Econ. Geol.*, **94,** 1051–1066.

**Lowe, D.R.** and **Braunstein, D.** (2003) Microstructure of high-temperature (>73 °C) siliceous sinter deposited around hot springs and geysers, Yellowstone National Park: the role of biological and abiological processes in sedimentation. *Can. J. Earth Sci.*, **40,** 1611–1642.

**McLennan, S.M.** (1989) Rare earth elements in sedimentary rocks: influence of provenance and sedimentary processes. *Reviews Mineral. Geochem.*, **21,** 169–200.

**Michard, A., Albarède, G., Michard, G., Minster, J.F.** and **Charlou, J.L.** (1983) Rare-earth elements and uranium in high-temperature solutions from East Pacific Rise hydrothermal vent field (13°N). *Nature*, **303,** 795–797.

**Mills, R.A.** and **Elderfield, H.** (1995) Rare earth element geochemistry of hydrothermal deposits from the active TAG Mound, 26°N Mid-Atlantic Ridge. *Geochim. Cosmochim. Acta*, **59,** 3511–3524.

**Monin, A.S., Plakhin, E.A., Podrazhansky, A.M., Sagalevich, A.M.** and **Sorkhtin, O.G.** (1981) Visual observations of the Red Sea hot brines. *Nature*, **291,** 222–225.

**Murray, R.W.** (1994) Chemical criteria to identify the depositional environment of chert: general principles and applications. *Sed. Geol.*, **90,** 213–232.

**Nijman, W., De bruijne, K.H.** and **Valkering, M.E.** (1998) Growth fault control of Early Archaean cherts, barite mounds and chert-barite veins, North Pole Dome, Eastern Pilbara, Westerm Australia. *Precambrian Res.*, **88,** 25–52.

**Owen, A.W., Armstrong, H.A.** and **Floyd, J.D.** (1999) Rare earth elements in chert clasts as provenance indicators in the Ordovician and Silurian of the Southern Uplands of Scotland. *Sed. Geol.*, **124,** 185–195.

**Peng, J., Xia, W.J.** and **Yi, H.S.** (1995) Silicon and oxygen isotopic compositions and origin of Late Precambrian bedded cherts in western Hunan. *Geol. Rev.*, **41** (1), 34–41 (in Chinese with English abstract).

**Resing, J.A., Lupton, J.E., Feely, R.A.** and **Lilley, M.D.** (2004) $CO_2$ and $^3He$ in hydrothermal plumes: implications for mid-ocean ridge $CO_2$ flux. *Earth Planet. Sci. Lett.*, **226,** 449–464.

**Schoell, M.** and **Hartmann, M.** (1978) Changing hydrothermal activity in the Atlantis II Deep geothermal system. *Nature*, **274,** 784–785.

**Schröder, S.** and **Grotzinger, J.P.** (2007) Evidence for anoxia at the Ediacaran–Cambrian boundary: the record of redox-sensitive trace elements and rare earth elements in Oman. *J. Geol. Soc. London*, **164,** 175–187.

**Shen, Y.** and **Shidlowski, M.** (2000) New C isotope stratigraphy from southwest China: implication for the placement of the Precambrian–Cambrian boundary on the Yangtze Platform and global correlations. *Geology*, **28,** 623–626.

**Steiner, M., Li, G.X., Qian, Y., Zhu, M.Y.** and **Erdtmann, B.D.** (2007) Neoproterozoic to Early Cambrian small shelly fossil assemblages and a revised biostratigraphic correlation of the Yangtze Platform (China). *Palaeogeogr. Palaeoclimatol. Palaeoecol.*, **254,** 67–99.

**Stüben, D., Taibi, N.E., McMurtry, G.M., Scholten, J., Stoffers, P.** and **Zhang, D.** (1994) Growth history of a hydrothermal silica chimney from the Marian back-arc spreading center (southwest Pacific, 18°13'N). *Chem. Geol.*, **113,** 273–296.

**Tang, S.R., Wang, D.A.** and **Li, R.W.** (1997) Organic petrology of the Cambrian-Sinian chert from the Xiangchuan region. *Acta Sediment. Sin.,* **15,** 54–59 (in Chinese with English abstract).

**Taylor, S.R.** and **McClennan, S.M.** (1985) *The Continental Crustal: Its Composition and Evolution*. Blackwell, Oxford, 312 pp.

**Tivey, M.K., Mills, R.A.** and **Teagle, D.A.H.** (1998) Temperature and salinity of fluid inclusions in anhydrite as indicators of seawater entrainment and heating the TAG active mounds, In: *Proc. ODP Scientific Results* (Eds P.M. Herzig, S.E. Humphris, D.J. Miller and R.A. Zierenberg), *Ocean Drilling Program*, College Station, TX, **158,** 179–190.

**Urabe, T.** and **Kusakabe, M.** (1990) Barite silica chimneys from the Sumisu Rift, Izu-Bonin Arc: possible analog to hematitic chert associated with Kuroko deposits. *Earth Planet. Sci. Lett.*, **100,** 283–290.

**Van Kranendonk, M.K.** (2006) Volcanic degassing, hydrothermal circulation and the flourishing of early life on Earth: a review of the evidence from c. 3490-3240 Ma rocks of the Pilbara Supergroup, Pilbara Craton, Western Australia. *Earth-Sci. Rev.*, **74,** 197–240.

**Vernhet, E.** and **Reijmer, J.J.G.** (2010) Sedimentary evolution of the Ediacaran Yangtze platform shelf (Hubei and Hunan provinces, Central China). *Sed. Geol.*, **225,** 99–115.

**Wang, Z.C.** and **Chu, X.L.** (1993) Strontium isotopic ratios of barite and witherite in Early Cambrian. *Chin. Sci. Bull.*, **38,** 1490–1492.

**Wang, Z.C.** and **Li, G.Z.** (1991) Barite and witherite deposits in Lower Cambrian shales of South China: stratigraphic distribution and geochemical characterization. *Econ. Geol.*, **86,** 354–363.

**Wang, J.** and **Li, Z.-X.** (2003) History of Neoproterozoic rift basins in South China: implications for Rodinia break-up. *Precambrian Res.*, **122,** 141–158.

**Winckler, G., Aeschbach-Hertig, W., Kipfer, R., Botz, R., Rübel, A.P., Bayer, R.** and **Stoffers, P.** (2001) Constraints on origin and evolution of Red Sea brines from helium and argon isotopes. *Earth Planet. Sci. Lett.*, **184,** 671–683.

**Xia, F., Ma, D.S., Pan, J.Y., Sun, Z.X., Cao, S.L., Nie, W.M.** and **Wu, K.** (2004) Strontium isotopic signature of hydrothermal sedimentation from Early Cambrian barite deposits in east Guizhou, China. *Chin. Sci. Bull.*, **49,** 2632–2636.

**Xue, Y.S., Tang, T.F.** and **Yu, C.L.** (1992) Paleokarst cave phosphorites of the Upper Sinian Dengying Formation in southern China. *Acta Sed. Sinica*, **10** (3), 145–153 (in Chinese with English abstract).

**Zheng, Y.-F., Wu, R.-X., Wu, Y.-B., Zhang, S.-B., Yuan, H.-L.** and **Wu, F.-Y.** (2008) Rift melting of juvenile arc-derived crust: geochemical evidence from Neoproterozoic volcanic and granitic rocks in the Jiangnan orogen, South China. *Precambrian Res.*, **163,** 351–383.

**Zhu, M.Y., Zhang, J.M., Steiner, M., Yang, A.H., Li, G.X.** and **Erdtman, B.D.** (2003) Sinian-Cambrian stratigraphic framework for shallow- to deep-water environments of the Yangtze Platform: an integated approach. *Progr. Natural. Sci.*, **13,** 951–960.

*Manuscript received 9 July 2010; revision accepted 4 July 2011*